Geophysical Prospecting, 2008, **56**, 395–417 doi:10.1111/j.1365-2478.2008.00697.x

Global-scale seismic interferometry: theory and numerical examples

Elmer Ruigrok*, Deyan Draganov and Kees Wapenaar

Department of Geotechnology, Delft University of Technology, P.O. Box 5048, 2600 GA Delft, The Netherlands

Received May 2007, revision accepted January 2008

ABSTRACT

Progress in the imaging of the mantle and core is partially limited by the sparse distribution of natural sources; the earthquake hypocenters are mainly along the active lithospheric plate boundaries. This problem can be approached with seismic interferometry. In recent years, there has been considerable progress in the development of seismic interferometric techniques. The term seismic interferometry refers to the principle of generating new seismic responses by cross-correlating seismic observations at different receiver locations. The application of interferometric techniques on a global scale could create sources at locations where no earthquakes occur. In this way, yet unknown responses would become available for the application of travel-time tomography and surface-wave dispersion studies. The retrieval of a dense-enough sampling of source gathers would largely benefit the application of reflection imaging.

We derive new elastodynamic representation integrals for global-scale seismic interferometry. The relations are different from other seismic interferometry relations for transient sources, in the sense that they are suited for a rotating closed system like the Earth. We use a correlation of an observed response with a response to which free-surface multiple elimination has been applied to account for the closed system. Despite the fact that the rotation of the Earth breaks source-receiver reciprocity, the seismic interferometry relations are shown to be valid. The Coriolis force is included without the need to evaluate an extra term.

We synthesize global-scale earthquake responses and use them to illustrate the acoustic versions of the new interferometric relations. When the sampling of real source locations is dense enough, then both the responses with and without free-surface multiples are retrieved. When we do not take into account the responses from the sources in the direct neighborhood of the seismic interferometry-constructed source location, the response with free-surface multiples can still be retrieved. Even when only responses from sources at a certain range of epicentral distances are available, some events in the Green's function between two receiver locations can still be retrieved. The retrieved responses are not perfect, but the artefacts can largely be ascribed to numerical errors. The reconstruction of internal events – the response as if there was a source and a receiver on (major) contrasts within the model – could possibly be of use for imaging.

With modelling it is possible to discover in which region of the correlation panel stationary phases occur that contribute to the retrieval of events. This knowledge opens up a new way of filtering out undesired events and of discovering whether specific events could be retrieved with a given source-receiver configuration.

*E-mail: e.n.ruigrok@tudelft.nl

1. INTRODUCTION

Seismic reflection imaging has proven to be the most successful technique for the exploration of oil and gas. For the application of this technique, the subsurface needs to be illuminated from many different angles. With the acquired responses a high-resolution image of the subsurface can be made. On the exploration scale, the illumination from many directions can be achieved by using a dense grid of controlled sources at the surface (dynamite, vibrators, air guns, etc.). On a global scale, though, one is dependent on the natural-source distribution. Only the larger earthquakes generate enough energy to illuminate the deep interior of the Earth. These larger earthquakes are mainly situated along the active lithospheric plate boundaries (Fig. 1). Thus, there are many areas on the globe, beneath which the Earth's interior is not directly illuminated. It is this sparse source distribution that especially impedes the use of seismic reflection imaging on a global scale. Also, to obtain a better laterally varying velocity model using travel-time tomography or surface-wave dispersion studies, more source locations are required. The shortage of source locations on a global scale can be reduced with seismic interferometry.

In recent years, there has been considerable progress in the development of seismic interferometry techniques, see the July/August 2006 issue of *Geophysics* for an overview. Seismic interferometry is a method by which additional information can be extracted from wavefield responses. The responses measured at any combination of two receiver locations can be combined with seismic interferometry to construct the response as if there were a source at one of the receiver locations and a receiver at the other. In this way, theoretically, a source can be created at any receiver position, provided there is enough illumination.

Seismic interferometry relations have been derived for two exploration-type configurations. The first configuration, for transient or noise sources in the subsurface, was introduced by Claerbout (1968) for 1D media and was proven to hold for a 3D arbitrary inhomogeneous medium by Wapenaar *et al.* (2002). These relations (for transient and for noise sources) were numerically validated by Draganov *et al.* (2004b) and successfully applied on real data by Draganov *et al.* (2007) for noise sources and by Shiraishi *et al.* (2006) for transient sources.

The other configuration, for controlled sources at the surface, was introduced by Schuster (2001). The technique, including an imaging step, was successfully applied on real data (Schuster *et al.* 2004). For the situation with receivers in a borehole, Bakulin and Calvert (2004) developed the 'virtual source method', by which the sources at the surface are redatumed through a complex overburden to the receiver positions in the borehole.

Independent of the developments in exploration geophysics, seismic interferometry was also introduced in the solid Earth community. The work was inspired by ultrasonic experiments performed by Weaver and Lobkis (2001) and by time-reversed acoustics experiments (Derode *et al.* 2003). Campillo and Paul (2003) used seismic interferometry to construct surface-wave Green's functions between pairs of station positions. They used the diffusive part of the coda information from earthquake responses. Other researchers (Shapiro *et al.* 2005; Gerstoft *et al.* 2006; Yao *et al.* 2006) also applied sesismic interferometry to retrieve surface-wave Green's functions on a regional scale. They used different source types and correlation

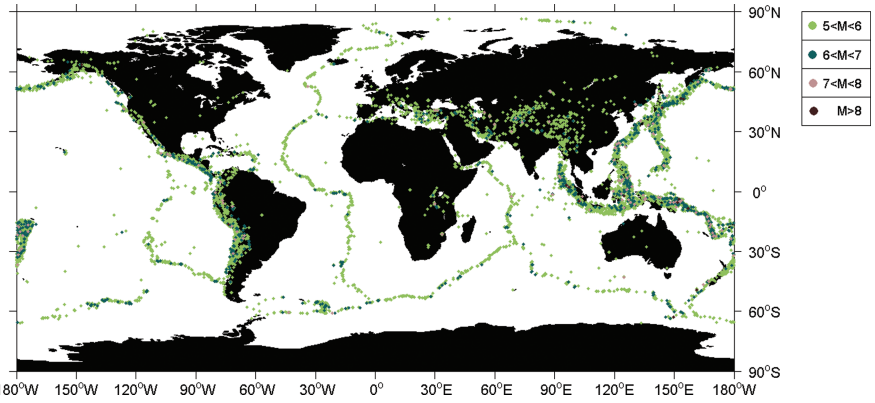

Figure 1 Distribution of the larger earthquakes over the globe, from 1997 to 2007. Over 15 000 earthquakes with magnitude greater than 5.0 are plotted with clubs, of which the colours depict the magnitude. The map was made with data from the USGS National Earthquake Information Center.

procedures. The retrieved Green's functions can be directly used to estimate velocity models of the crust and upper mantle with travel-time tomography and surface-wave dispersion studies.

Another application of seismic interferometry in solid Earth research was introduced by Schuster *et al*. (2004). They showed a synthetic example of applying seismic interferometry and an imaging step on scattered teleseismic arrivals. They used the first reverberations of an incoming wavefront between the free surface and large crustal interfaces. This application has the same configuration as the exploration-scale case with transient or noise sources in the subsurface. The main difference is the scale. Also, Shragge *et al*. (2006), Fan *et al*. (2006), Kumar and Bostock (2006) and Abe *et al*. (2007) applied seismic interferometry on regional-scale seismology using scattered teleseismic arrivals.

Seismic interferometry has not yet been applied in global-scale body-wave seismology. The application of seismic interferometry on a global scale would reconstruct the responses from sources at locations where no earthquakes occur. Since the locations of the receivers are exactly known, so are the locations of the retrieved sources. This is not the case for real earthquakes, for which there is an uncertainty of the exact source locations. For example, seismic interferometry could be applied on data from the USArray, of which the design is discussed in Levander (2003). Using seismic interferometry, new source positions could be retrieved at any of the receiver positions. In this way, yet unknown responses become available for the application of travel-time tomography. The retrieval of a dense-enough sampling of source gathers would largely benefit the application of seismic reflection imaging, with which a much better image of the deep interior could be obtained.

As noted above, exact seismic interferometry relations for transient sources were derived for exploration-type configurations (Wapenaar and Fokkema 2006). Wave phenomena on the scale of the entire Earth cannot be described by these configurations. The main reason is the presence of a closed free surface, which traps the energy.

Weaver and Lobkis (2001) derived an interferometric relation for a diffuse wavefield in a closed system. They performed an experiment with random sources (acoustic thermal fluctuations in an ultrasonic experiment) placed throughout a volume. The Earth is not filled with random sources, at least not with sources exciting waves in the frequency bandwidth that is used in global seismology. Hence, the wavefield in the Earth is far from diffuse. Moreover, the noise sources near the surface (ocean-wave motion, etc.) do not excite enough energy to illuminate the very deep contrasts like the core-mantle boundary.

Table 1 Terminology, solid Earth versus exploration-scale seismology

solid Earth	**exploration**
source time function	source wavelet
epicentral distance	offset
seismogram	trace
station	receiver
seismic event	source
phase	event

In this paper, we derive elastodynamic global-scale interferometric relations for transient sources (earthquakes) near the enclosing surface of the medium (the Earth's free surface). In this derivation, we take the rotation of the Earth into account. The acoustic versions of the relations are numerically validated with synthesized global-scale earthquake responses. Besides illustrating the derived relations numerically, we also use the synthesized responses to test one of the relations for more realistic situations, namely suboptimal source sampling and responses only from sources at a specific range of epicentral distances.

The terminology used in exploration-scale seismology is sometimes different from that used in solid Earth seismology (Table 1). In this paper, no explicit choice has been made between the two. However, to avoid confusion we hereafter use the exploration terms 'source' and 'event' instead of the solid-Earth terms 'seismic event' and 'phase', respectively.

2. DERIVATION OF GLOBAL-SCALE SEISMIC INTERFEROMETRY RELATIONS

In this section, we derive and clarify global-scale seismic interferometry relations for transient sources near the surface. First the correlation-type reciprocity theorem is derived. Subsequently it is used to derive a global-scale seismic interferometry relation that takes the rotation of the Earth and the Coriolis force into account. Afterwards we make a small adjustment to handle the absence of near-offset responses, as is common in the real Earth situation. With near-offset responses we mean the responses due to the sources which are in the direct neighbourhood of the receiver location where we want to reconstruct a source. At the end of this section we present the acoustic versions of the derived relations.

2.1. Elastodynamic reciprocity theorem

We start with the derivation of the correlation-type elastodynamic reciprocity theorem in the frequency domain. A similar derivation (but without Coriolis force) can be found in

Wapenaar and Fokkema (2006). The temporal Fourier transform of a space- and time-dependent quantity $p(\mathbf{x}, t)$ is defined as

$$\hat{p}(\mathbf{x}, \omega) = \int_{-\infty}^{\infty} p(\mathbf{x}, t) e^{-j\omega t} dt, \tag{1}$$

where j is the imaginary unit and ω is the angular frequency. The hat above the quantities denotes that they are in the frequency domain. $\mathbf{x} = (x_1, x_2, x_3)$ denotes the position vector.

A reciprocity theorem relates two independent states in one and the same domain (de Hoop 1988; Fokkema and van den Berg 1993). Here we relate two elastodynamic states denoted by A and B. State A is characterized by the source state, material state and wavefield state. The source state defines the types, locations and timings of sources within the domain $\mathbb{D}$. The material state gives the relevant material properties within $\mathbb{D}$. In the elastodynamic case, these properties are mass density ρ and compliance s_{ijkl}. The wavefield state is an expression of the waves that exist within $\mathbb{D}$ due to sources within, on the boundary of, or outside the domain $\mathbb{D}$. The wavefield is characterized by the stress tensor $\tau_{ij}(\mathbf{x}, t)$ and the particle velocity $v_i(\mathbf{x}, t)$. The stress tensor and the particle velocity are coupled by the equation of motion, written in the space-frequency domain as (Dahlen and Tromp 1998)

$$j\omega\hat{\rho}\hat{v}_i - \partial_j\hat{\tau}_{ij} + 2\hat{\rho}\epsilon_{ijk}\Omega_j\hat{v}_k = \hat{f}_i, \tag{2}$$

and the linearized stress-strain relation:

$$-j\omega\hat{s}_{ijkl}\hat{\tau}_{kl} + (\partial_j\hat{v}_i + \partial_i\hat{v}_j)/2 = \hat{h}_{ij}, \tag{3}$$

where ∂_j denotes differentiation with respect to the spatial coordinates and ϵ_{ijk} is the Levi-Cevita operator, $\epsilon_{ijk} = 1$ when $ijk = 123; 231; 312$, $\epsilon_{ijk} = -1$ when $ijk = 132; 213; 321$, while $\epsilon_{ijk} = 0$ otherwise. For repeated Latin subscripts Einstein's summation convention applies. In equation (2) the third term on the left-hand side is the apparent Coriolis force for a solid rotation with angular velocity Ω_j and $\hat{f}_i(\mathbf{x}, \omega)$ is the external volume force density. In equation (3) $\hat{h}_{ij}(\mathbf{x}, \omega)$ is the external deformation rate density. In equations (2) and (3) the medium parameters $\hat{\rho}$ and $\hat{s}_{ijkl}$ are, for the moment, frequency dependent and complex valued and thus account for inelastic losses in the medium.

We use the integral theorem of Gauss for any continuously differentiable vector function $\hat{p}_j$:

$$\oint_{\partial\mathbb{D}} \hat{p}_j n_j d^2\mathbf{x} = \int_{\mathbb{D}} \partial_j \hat{p}_j d^3\mathbf{x}, \tag{4}$$

where $\partial\mathbb{D}$ is the boundary of $\mathbb{D}$ and n_j is the outward-pointing unit vector normal to $\partial\mathbb{D}$ (Fig. 2), $d^3\mathbf{x}$ the elementary volume in 3-dimensional Euclidean space and $d^2\mathbf{x}$ the elementary area of $\partial\mathbb{D}$.

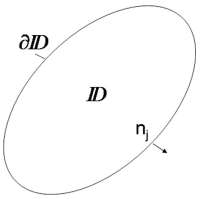

Figure 2 Configuration for the application of Gauss' integral theorem and for relations derived from Gauss' integral theorem. It depicts the volume of integration, domain $\mathbb{D}$, enclosed by the surface of integration, $\partial\mathbb{D}$ and the outward pointing normal vector n_j.

For $\hat{p}_j$ we choose an interaction function between the wavefield quantities of two elastodynamic states, denoted by A and B, respectively:

$$\hat{p}_j = -\hat{v}^*_{i,A}\hat{\tau}_{ij,B} - \hat{\tau}^*_{ij,A}\hat{v}_{i,B}, \tag{5}$$

in which * denotes complex conjugation and $\hat{\tau}_{ij,A}/\hat{\tau}_{ij,B}$ and $\hat{v}_{i,A}/\hat{v}_{i,B}$ denote the stress tensor and particle velocity of state A/B, respectively. Substituting equation (5) into Gauss' integral theorem, applying the product rule for differentiation for the integrand of the volume integral, substituting equations (2) and (3) or their complex conjugated versions to replace $\partial_j\hat{\tau}^*_{ij,A}$, $\partial_j\hat{\tau}_{ij,B}$, $\partial_j\hat{v}^*_{i,A}$ and $\partial_j\hat{v}_{i,B}$, using the symmetry relations $s_{ijkl} = s_{klij}$ and $\tau_{ij} = \tau_{ji}$ and finally reordering the terms in integrals containing medium-parameter terms, source terms and Coriolis terms, yields

$$\begin{aligned}
&\oint_{\partial\mathbb{D}} \{-\hat{v}^*_{i,A}\hat{\tau}_{ij,B} - \hat{\tau}^*_{ij,A}\hat{v}_{i,B}\} n_j d^2\mathbf{x} \\
&\quad = -j\omega \int_{\mathbb{D}} \{\hat{\tau}^*_{ij,A}(\hat{s}_{ijkl,B} - \hat{s}^*_{ijkl,A})\tau_{kl,B} + \hat{v}^*_{i,A}(\hat{\rho}_B - \hat{\rho}^*_A)\hat{v}_{i,B}\} d^3\mathbf{x} \\
&\qquad + \int_{\mathbb{D}} \{-\hat{\tau}^*_{ij,A}\hat{h}_{ij,B} + \hat{v}^*_{i,A}\hat{f}_{i,B} - \hat{h}^*_{ij,A}\hat{\tau}_{ij,B} + \hat{f}^*_{i,A}\hat{v}_{i,B}\} d^3\mathbf{x} \\
&\qquad - \int_{\mathbb{D}} \{2\hat{\rho}^*_A\epsilon_{ijk}\hat{v}_{i,B}\Omega_{j,A}\hat{v}^*_{k,A} + 2\hat{\rho}_B\epsilon_{ijk}\hat{v}^*_{i,A}\Omega_{j,B}\hat{v}_{k,B}\} d^3\mathbf{x}.
\end{aligned} \tag{6}$$

Equation (6) is the Rayleigh-Betti reciprocity theorem of the correlation type accounting for the Coriolis force.

From here onwards we take the material state for states A and B equal and we consider lossless media. Hence $\hat{\rho}^*_A = \hat{\rho}_B = \rho$ and $\hat{s}^*_{ijkl,A} = \hat{s}_{ijkl,B} = s_{ijkl}$. As a result the integral with the medium-contrast interactions in equation (6) – the first integral on the right-hand side of the equation – vanishes.

For the application to global-scale wave phenomena we choose $\Omega_{j,A} = \Omega_{j,B} = \Omega_j$, which is the solid rotation of the Earth. The integral with the Coriolis terms in equation (6) - the third integral on the right-hand side of the equation – can

now be rewritten as

$$-\int_{\mathbb{D}}\{2\rho(\epsilon_{ijk}\hat{v}_{i,B}\Omega_j\hat{v}^*_{k,A}+\epsilon_{ijk}\hat{v}^*_{i,A}\Omega_j\hat{v}_{k,B})\}d^3\mathbf{x}. \quad (7)$$

Using the property $\epsilon_{ijk}=-\epsilon_{kji}$ we may rewrite the last term under the integral as $-\epsilon_{ijk}\hat{v}^*_{k,A}\Omega_j\hat{v}_{i,B}$. Hence the third integral on the right-hand side of equation (6) vanishes as well.

Consequently, for a solid rotating lossless Earth the Rayleigh-Betti reciprocity theorem of the correlation type accounting for Coriolis force becomes

$$\oint_{\partial\mathbb{D}}\{-\hat{v}^*_{i,A}\hat{\tau}_{ij,B}-\hat{\tau}^*_{ij,A}\hat{v}_{i,B}\}n_j d^2\mathbf{x} = \int_{\mathbb{D}}\{-\hat{\tau}^*_{ij,A}\hat{b}_{ij,B}+\hat{v}^*_{i,A}\hat{f}_{i,B}-\hat{b}^*_{ij,A}\hat{\tau}_{ij,B}+\hat{f}^*_{i,A}\hat{v}_{i,B}\}d^3\mathbf{x}, \quad (8)$$

in which – surprisingly – no term is needed to account for the Coriolis force.

Fokkema and van den Berg (1993) related different acoustic states with the help of the acoustic version of equation (8), without considering rotation. By doing so, useful relations were derived for seismic applications. Following a similar procedure, both acoustic and elastodynamic relations for seismic interferometry were derived by Wapenaar and Fokkema (2006). Snieder (2007) used the acoustic version of equation (6) without considering rotation and without a complex density but instead with a complex-valued compressibility to derive interferometric relations for dissipative acoustic media.

2.2. Basic relation

The representations for states A and state B are depicted in Fig. 3. States A and B are so-called Green's states: the sources are assumed to be impulses, such that the responses can be written as impulse responses or Green's functions. To link reality with a Green's state, a wavefield registration would need to be deconvolved for the source wavelet.

Figure 3(a) depicts the representation for state A. Domain $\mathbb{D}$ covers the entire inner space of the Earth. The boundary surface $\partial\mathbb{D}$ of $\mathbb{D}$ coincides with the Earth's surface. A shallow-depth earthquake (source) has a hypocenter at $\mathbf{x}_A$, which is approximately at the Earth's surface. The source in state A is represented as a boundary condition for the traction at the free surface. The boundary condition for approaching the free surface (denoted as FS) from its interior (Earth) is

$$\lim_{\mathbf{x}\uparrow\mathbf{x}_{\mathrm{FS}}}\hat{\tau}_{ik}(\mathbf{x})n_k=\delta(\mathbf{x}-\mathbf{x}_A)\delta_{ip} \quad \text{for} \quad \mathbf{x}\in\partial\mathbb{D}, \quad (9)$$

in which n_k denotes the outward pointing normal vector as depicted in Fig. 2 and δ_{ip} is the Kronecker delta function, $\delta_{ip}=0$ for $i\neq p$, $\delta_{ip}=1$ for $i=p$. The Dirac delta function on the right-hand side of equation (9) is a 2D delta function in the tangential directions.

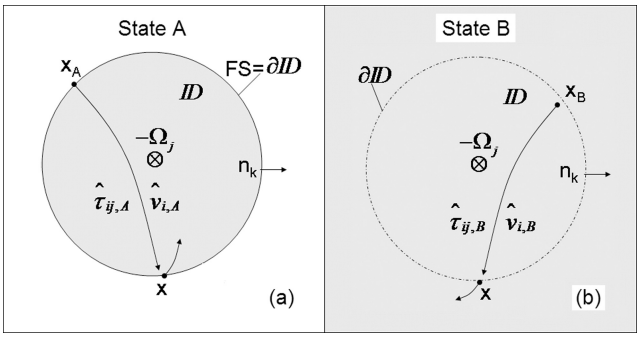

Figure 3 Location of $\mathbf{x}_A$, $\mathbf{x}_B$ and $\mathbf{x}$ on a simplified Earth model, with rotation Ω_j opposite to the actual Earth's rotation. A domain $\mathbb{D}$ enclosed by a surface $\partial\mathbb{D}$ covers the entire inner space of the Earth, hence $\partial\mathbb{D}$ coincides with the free surface (denoted as FS). $\hat{\tau}_{ij}$ and $\hat{v}_i$ describe the wavefields within $\mathbb{D}$ and at $\partial\mathbb{D}$ due to a source at $\mathbf{x}_A$ or $\mathbf{x}_B$. (a) State A, Earth with free surface (FS); $\mathbf{x}_A$ lies approximately at $\partial\mathbb{D}$. (b) State B, Earth without free surface; $\mathbf{x}_B$ lies just within $\mathbb{D}$.

Figure 3(b) depicts the representation for state B. A shallow-depth earthquake has a hypocenter at $\mathbf{x}_B$, which is just within $\mathbb{D}$. This earthquake is assumed to be a deformation-rate source. State B is a representation for an Earth without free surface. The response of state B can be obtained from a real Earth response by using, e.g., surface-related multiple elimination (SRME) (Berkhout and Verschuur 1997; Verschuur and Berkhout 1997).

The choices made above for the type of earthquake sources are not unique. Other source mechanisms can be dealt with but will not be considered in this paper.

The choice to include one state with free surface and one without is not arbitrary. If we chose both states to include a free surface there would be no integral left to be evaluated in equation (8). If we removed the free surface in both states, then there would be no reflections at the free surface, which are necessary for the retrieval of a response with seismic interferometry.

States A and B are representations of an Earth that is rotating in the opposite direction as compared to the actual rotation of the Earth Ω_j (Fig. 3). This choice will become clear later.

The mathematical expressions for the two elastodynamic states are listed in Table 2. States A and B are defined for one and the same lossless inhomogeneous elastodynamic medium. The wavefield quantities, $\hat{\tau}_{ij}$ and $\hat{v}_i$, can be represented as Green's functions everywhere within $\mathbb{D}$ and for state B also everywhere at $\partial\mathbb{D}$. In state A, at the free surface, we can only

Table 2 States for the elastodynamic reciprocity theorem, in which the source state is a representation for relatively shallow earthquakes.

		State *A*: free surface	State *B*: no free surface
wavefield	$\hat{\tau}_{ij}$	$\hat{G}^{\tau,\tau}_{ij,p}(\mathbf{x}, \mathbf{x}_A, \omega \mid -\mathbf{\Omega})$	$\hat{\bar{G}}^{\tau,h}_{ij,qr}(\mathbf{x}, \mathbf{x}_B, \omega \mid -\mathbf{\Omega})$
$\mathbf{x} \in \mathbb{D}$	$\hat{v}_i$	$\hat{G}^{v,\tau}_{i,p}(\mathbf{x}, \mathbf{x}_A, \omega \mid -\mathbf{\Omega})$	$\hat{\bar{G}}^{v,h}_{i,qr}(\mathbf{x}, \mathbf{x}_B, \omega \mid -\mathbf{\Omega})$
wavefield	$\hat{\tau}_{ik}n_k$	$\delta(\mathbf{x} - \mathbf{x}_A)\delta_{ip}$	$\hat{\bar{G}}^{\tau,h}_{i,qr}(\mathbf{x}, \mathbf{x}_B, \omega \mid -\mathbf{\Omega})$
$\mathbf{x} \in \partial\mathbb{D}$	$\hat{v}_i$	$\hat{G}^{v,\tau}_{i,p}(\mathbf{x}, \mathbf{x}_A, \omega \mid -\mathbf{\Omega})$	$\hat{\bar{G}}^{v,h}_{i,qr}(\mathbf{x}, \mathbf{x}_B, \omega \mid -\mathbf{\Omega})$
source	$\hat{h}_{ij}$	0	$\delta(\mathbf{x} - \mathbf{x}_B)\delta_{iq}\ \delta_{jr}$
$\mathbf{x} \in \mathbb{D}$	$\hat{f}_i$	0	0

have a traction vector $\hat{\tau}_{ik}n_k$ unequal to zero at the location of the source. However, because the free surface can move freely, $\hat{v}_i$ can be non-zero everywhere at $\partial\mathbb{D}$. The source in state *B* is represented in the source state. Here the Dirac delta function is a 3D delta function.

The first and second superscripts of the Green's function $\hat{G}$ denote, respectively, the observed response type (τ – stress tensor; v – particle velocity) and the source type (τ – traction source; h – deformation-rate source). The subscripts denote the components of the observed response and the source, respectively. When only one subscript belongs to the traction or deformation-rate source, it is a traction or deformation-rate vector acting on a plane tangential to the free surface. The bar in state *B* denotes a response without free surface multiples. When the bar is omitted (as in state *A*) we mean the complete Green's function, including all free surface multiples. $\hat{G}(\mathbf{x}, \mathbf{x}_A, \omega \mid -\mathbf{\Omega})$ is the response observed at $\mathbf{x}$ due to a source at $\mathbf{x}_A$, given as a function of frequency ω, for a rotating medium minus the angular velocity of the Earth, $-\mathbf{\Omega}$.

We substitute the expressions of Table 2 into equation (8). Making use of the sifting property of the delta function and the multiplication property of the Kronecker delta function, we obtain:

$$-\oint_{\partial\mathbb{D}} \left\{\hat{G}^{v,\tau}_{i,p}(\mathbf{x}, \mathbf{x}_A, \omega \mid -\mathbf{\Omega})\right\}^* \hat{\bar{G}}^{\tau,h}_{i,qr}(\mathbf{x}, \mathbf{x}_B, \omega \mid -\mathbf{\Omega}) d^2\mathbf{x} = -\left\{\hat{G}^{\tau,\tau}_{qr,p}(\mathbf{x}_B, \mathbf{x}_A, \omega \mid -\mathbf{\Omega})\right\}^* + \hat{\bar{G}}^{v,h}_{p,qr}(\mathbf{x}_A, \mathbf{x}_B, \omega \mid -\mathbf{\Omega}). \quad (10)$$

We change the integration over receiver positions to an integration over source positions by applying the generalized source-receiver reciprocity relations for the Green's functions. In a rotating medium the usual source-receiver reciprocity relation breaks down, hence

$$\hat{G}(\mathbf{x}_B, \mathbf{x}_A, \omega \mid \mathbf{\Omega}) \neq \hat{G}(\mathbf{x}_A, \mathbf{x}_B, \omega \mid \mathbf{\Omega}). \quad (11)$$

However, in Appendix A it is shown that generalized source-receiver reciprocity relations, with opposite rotation, do hold:

$$\hat{G}(\mathbf{x}_B, \mathbf{x}_A, \omega \mid \mathbf{\Omega}) = \hat{G}(\mathbf{x}_A, \mathbf{x}_B, \omega \mid -\mathbf{\Omega}). \quad (12)$$

Thus, by using the generalized source-receiver reciprocity relation, equations (A6), (A9), (A4) and (A8) and subsequently applying the inverse Fourier transform, we obtain the following expression in the time domain:

$$\oint_{\partial\mathbb{D}} G^{v,\tau}_{p,i}(\mathbf{x}_A, \mathbf{x}, -t \mid \mathbf{\Omega}) * \bar{G}^{\tau,h}_{qr,i}(\mathbf{x}_B, \mathbf{x}, t \mid \mathbf{\Omega}) d^2\mathbf{x} = G^{v,h}_{p,qr}(\mathbf{x}_A, \mathbf{x}_B, -t \mid \mathbf{\Omega}) - \bar{G}^{\tau,f}_{qr,p}(\mathbf{x}_B, \mathbf{x}_A, t \mid \mathbf{\Omega}), \quad (13)$$

in which $*$ denotes convolution. Equation (13) is the basic global-scale seismic interferometry relation for the actual rotating Earth. It states that we can reconstruct Green's functions between receiver position $\mathbf{x}_A$ and $\mathbf{x}_B$ in a rotating Earth when we cross-correlate responses at $\mathbf{x}_A$ and $\mathbf{x}_B$ resulting from sources at all $\mathbf{x}$ on $\partial\mathbb{D}$ and subsequently integrate along these sources.

We have shown here that the Green's function retrieval is in principle also valid for rotating media. Similar to flow, as discussed by Wapenaar (2006), rotation breaks time reversal and source-receiver reciprocity but does not break Green's function retrieval by seismic interferometry.

2.3. Relation without near-offset responses

In the previous section, we derived an seismic interferometry relation that contains an integration over responses from sources all around the globe. In reality, one would like to simulate a source on a place where no earthquakes occur. This would mean that at least the near-offset responses are missing.

To evaluate what happens if we cannot integrate over the near-offset part, we divide the integration surface $\partial\mathbb{D}$ in a near-offset part $\partial\mathbb{D}_0$ with respect to $\mathbf{x}_A$ and the remaining surface $\partial\mathbb{D}_1$:

$$\partial\mathbb{D} = \partial\mathbb{D}_0 + \partial\mathbb{D}_1. \quad (14)$$

We substitute the expressions of Table 2 into equation (8), apply the sifting property for the Delta function and the multiplication property of the Kronecker Delta function in the volume integral and replace the complete surface integral by

an integration over $\partial\mathbb{D}_1$, yielding:

$$\int_{\partial\mathbb{D}_1} \delta(\mathbf{x}-\mathbf{x}_A)\delta_{ip}\hat{\bar{G}}^{\nu,h}_{i,qr}(\mathbf{x},\mathbf{x}_B,\omega\mid-\boldsymbol{\Omega})d^2\mathbf{x} + \int_{\partial\mathbb{D}_1}\{\hat{G}^{\nu,\tau}_{i,p}(\mathbf{x},\mathbf{x}_A,\omega\mid-\boldsymbol{\Omega})\}^*\hat{\bar{G}}^{\tau,h}_{i,qr}(\mathbf{x},\mathbf{x}_B,\omega\mid-\boldsymbol{\Omega})d^2\mathbf{x} \approx \{\hat{G}^{\tau,\tau}_{qr,p}(\mathbf{x}_B,\mathbf{x}_A,\omega\mid-\boldsymbol{\Omega})\}^*. \quad (15)$$

By not including the integration over $\partial\mathbb{D}_0$, we do not perfectly satisfy the representation in Table 2. Thus, equation (15) is not exact.

Since $\partial\mathbb{D}_1$ does not include $\mathbf{x}_A$, $\delta(\mathbf{x}-\mathbf{x}_A)$ is zero for all $\mathbf{x}\in\partial\mathbb{D}_1$ and the first term on the left-hand side of equation (15) vanishes. We apply generalized source-receiver reciprocity relations for Green's function equations (A6), (A9) and (A4). Subsequently applying the inverse Fourier transform, we obtain the following expression in the time domain:

$$\int_{\partial\mathbb{D}_1} G^{\nu,\tau}_{p,i}(\mathbf{x}_A,\mathbf{x},-t\mid\boldsymbol{\Omega})*\bar{G}^{\tau,h}_{qr,i}(\mathbf{x}_B,\mathbf{x},t\mid\boldsymbol{\Omega})d^2\mathbf{x} \approx G^{\nu,h}_{p,qr}(\mathbf{x}_A,\mathbf{x}_B,-t\mid\boldsymbol{\Omega}). \quad (16)$$

Equation (16) states that, when no measurements of near sources are available, we can only reconstruct the Green's function $G^{\nu,h}_{p,qr}(\mathbf{x}_A,\mathbf{x}_B,-t\mid\boldsymbol{\Omega})$, which contains the free surface multiples. The part of the response that is accurately reconstructed depends on the stationary points that are included in the integration and hence it depends on the size of $\partial\mathbb{D}_1$.

2.4 Acoustic relations

For acoustic media the wavefield is characterized by the pressure $p(\mathbf{x},t)$ and particle velocity $v_i(\mathbf{x},t)$. The pressure and the particle velocity are coupled by the linearized equation of motion, written in the space-frequency domain as:

$$j\omega\hat{\rho}\hat{v}_i+\partial_i\hat{p}+2\hat{\rho}\epsilon_{ijk}\Omega_j\hat{v}_k=\hat{f}_i \quad (17)$$

and the linearized stress-strain relation:

$$j\omega\hat{\kappa}\,\hat{p}+\partial_i\hat{v}_i=\hat{q}. \quad (18)$$

In equation (17), the apparent Coriolis force is again included for a solid rotation with angular velocity Ω_j. In equation (18), $\hat{\kappa}$ is the compressibility, which is frequency dependent and complex valued to account for inelastic losses in the medium and $\hat{q}$ is the volume source density of the volume injection rate.

Following the same approach as in section 2.2.1 but applying the Gauss theorem on the interaction function between two acoustic states A and B:

$$\hat{p}^*_A\hat{v}_{i,B}+\hat{v}^*_{i,A}\hat{p}_B, \quad (19)$$

and substituting equations (17) and (18) in the resulting expression, the acoustic correlation-type reciprocity theorem can be derived. Substituting the acoustic counterparts of states A and B, as listed in Table 2, into the acoustic correlation-type reciprocity theorem and by applying the generalized acoustic source-receiver reciprocity relations, equations (A14)–(A17), the acoustic global-scale seismic interferometry relations can be derived. Alternatively, we can directly rewrite the elastic seismic relations, equations (13) and (16), by replacing the superscripts h by q, τ by p and omitting all the subscripts. Note that, comparing equations (17) and (18) with equations (2) and (3), the sign of the pressure is defined opposite to that of the stress tensor. Thus, every time we replace τ by p we also need to introduce a minus sign. By doing so, the acoustic global-scale seismic interferometry relation reads

$$\oint_{\partial\mathbb{D}} G^{\nu,p}(\mathbf{x}_A,\mathbf{x},-t\mid\boldsymbol{\Omega})*\bar{G}^{p,q}(\mathbf{x}_B,\mathbf{x},t\mid\boldsymbol{\Omega})d^2\mathbf{x} = G^{\nu,q}(\mathbf{x}_A,\mathbf{x}_B,-t\mid\boldsymbol{\Omega})+\bar{G}^{p,f}(\mathbf{x}_B,\mathbf{x}_A,t\mid\boldsymbol{\Omega}) \quad (20)$$

and the acoustic global-scale seismic interferometry relation without near offset reads

$$\int_{\partial\mathbb{D}_1} G^{\nu,p}(\mathbf{x}_A,\mathbf{x},-t\mid\boldsymbol{\Omega})*\bar{G}^{p,q}(\mathbf{x}_B,\mathbf{x},t\mid\boldsymbol{\Omega})d^2\mathbf{x} \approx G^{\nu,q}(\mathbf{x}_A,\mathbf{x}_B,-t\mid\boldsymbol{\Omega}), \quad (21)$$

where ν and f are in the direction perpendicular to the free surface.

In the following we will take $\boldsymbol{\Omega}=0$.

3. GLOBAL-SCALE ACOUSTIC WAVEFIELD MODELLING

In the previous section, we derived relations for obtaining new seismic responses from the correlation of existing global-scale responses. This section deals with the generation of global-scale synthetic earthquake responses (seismograms) with which we can illustrate the derived relations.

We synthesize the seismograms with a simplified 2D acoustic lossless Earth model based on the Preliminary Reference Earth Model (PREM, Dziewonski and Anderson (1981)). The medium parameters vary only in the radial direction (r). The rotation of the Earth is neglected. Locations on the 2D Earth model are given as a function of radius and epicentral distance (Δ), ranging from -180 to 180°.

Figure 4(a) shows a graph of the PREM model P-wave velocity c_P and density ρ as a function of the radius of the Earth. The radius is zero at the centre of the Earth and increases to an average thickness of 6371 km at the Earth's surface. Figure 4(b) shows our simplified version of the PREM model.

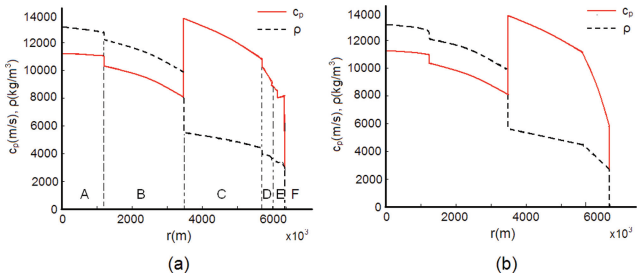

Figure 4 (a) The compressional-wave velocity c_p and density ρ as functions of the radius r. Values were taken from the PREM model. With increasing r, subsequently the inner core (denoted with A), outer core (B), lower mantle (C), transition zone (D), asthenosphere and lithosphere (E) and atmosphere (F) are encountered. (b) To create this smoothed version of the PREM model the discontinuities in the transition zone, upper mantle and crust were omitted.

As compared to the original PREM model the outermost 3 km were removed and the discontinuities in the crust and upper mantle were taken away.

We model the wavefield with a staggered finite-difference scheme of the acoustic wave equation (Virieux 1986). To enable the 2D finite difference modeling, the PREM model is transformed into a 2D rectangular gridded velocity and density model. We choose the grids small enough (2 × 2 km) to obviate grid dispersion and ensure stability by satisfying the criteria as derived in Lines *et al.* (1999).

Finite difference is not the most accurate technique available for synthesizing global-scale seismograms. However, it is the method of choice for our illustration, since consequent inaccuracies are of no harm and the computational affordability and easy adjustability make it a practical scheme to implement.

We generate the responses for state *B* with the same model as for state *A* but with the free surface removed. Different sources and receivers are placed in the model to generate all the responses that occur in the acoustic global scale seismic interferometry relations, equations (20) and (21). As a source wavelet we use the first derivative of a Gaussian wavelet, with a peak frequency at 0.156 Hz.

A source is initiated at $\Delta = 0^\circ$ at zero time. Every 0.05 s new values for the wavefield are calculated at every grid point. Starting at 200 s, a snapshot is taken every 300 s from the pressure at every grid point. Figure 5 shows the evolving pressure distribution throughout the model for state A. The wavefield can be seen to propagate only within the Earth due to the presence of a free surface. The wavefield after 200 s (upper left panel) is not perfectly circular due to the increasing velocity gradient in the crust and mantle. The wavefield is propagating much more slowly in the transverse direction than in the radial direction. Due to this, part of the wavefield starts to propagate along rays that bend towards the free surface. After 500 s (the upper middle panel) a part of the wavefield has already reflected a few times from the free surface. In the same panel, the reflection from the core-mantle boundary almost hits the free surface. Also, in this panel, the transmitted wavefield travelling in the radial direction is on its way through the inner core. On the subsequent panels the interaction of the wavefield with the different boundaries results in more and more events. The most pronounced are the free surface reflections of the direct wave.

From $\Delta = -180^\circ$ to 180° receivers are placed in the model. In total there are 2880 receivers which corresponds to one receiver per 0.125° or 14 km. Every 0.4 s the wavefield is registered at the grid points where the receivers are placed. Figure 6(a) shows the v-registrations of the receivers for state A and Fig. 6(b) shows the v-registrations for state *B*. The first 3000 s of the registrations are plotted. Only the responses for receivers between $\Delta = 0^\circ$ and 180° are shown. The other 180° of responses are identical because an axi-symmetric model is used. The kinematics of the arrivals can clearly be seen. The amplitude is shown as a colour variation from negative (blue) to zero (white) and positive (red). With the current plotting resolution, the true amplitude variation cannot be distinguished. High amplitudes were clipped, such that lower-amplitude arrivals can still be distinguished. The kinematics of the p-response of state *A* (measured just below the free surface) and state *B* look identical with the v-response. For this reason the p-responses are not shown here.

We compare our finite difference numerical results with arrival times generated by ray tracing. The computed ray-tracing arrival-times (Knapmeyer 2004) are plotted, with green crosses, in the same figure (Fig. 6). The events are assigned names according to the conventional (IASPEI) nomenclature (Storchak *et al.* 2003).

Generally, we see a good correspondence between the finite difference-modelled response and the ray-tracing arrival times. Since the finite difference modelling uses an adjusted version of the PREM model (Fig. 4b) whereas the ray tracing uses the original PREM model (Fig. 4a), the travel-time correspondence is of course not perfect.

The finite difference-modelled response for state A (Fig. 6a) contains very-high-order free surface multiples. The infinite-order free surface multiple is a surface wave. This linear event is denoted by 'L'. In the actual Earth the high-order free surface multiples cannot be distinguished. This notable difference is because the model we use is 2D and lossless and without the discontinuities in the upper mantle

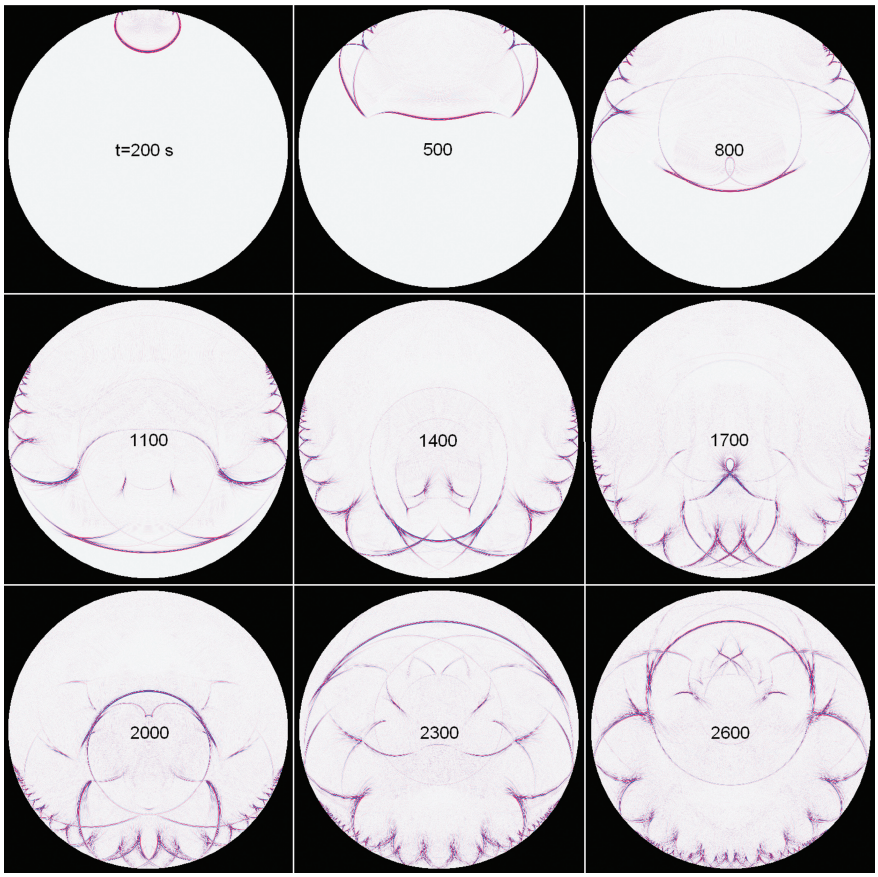

Figure 5 Snapshots of the wavefield spreading through the smoothed PREM model (for state A). The wavefield was initiated by an effective dipole source at 4 km depth. The snapshots were taken at 200, 500, 800, 1100, 1400, 1700, 2000, 2300 and 2600 seconds, respectively.

and crust. Another difference is that refractions, e.g., Pc, are modelled with faster amplitude decay than they have in the real Earth. This is an artefact of the usage of a rectangular grid. Because of this rectangular grid the interface is not just discontinuous in the radial direction but also contains little variations in the tangential direction by which a wave traveling along the interface is scattered.

In the finite difference-modelled response for state *B* (Fig. 6b), the reflection due to the change in velocity/density gradient at 570 km depth (Fig. 4) can be seen. It is labelled with 'a1'. Additionally, low-frequency reflections can be seen, which are labelled with 'a2'. These are artefacts of the absorbing taper at the edges of the model. They were largely filtered out by the application of a high-pass filter.

4. NUMERICAL ILLUSTRATION

In section 2, two relations for global-scale seismic interferometry were derived. Central in both relations is the correlation integral:

$$\oint_{\partial\mathbb{D}} G^{\nu,p}(\mathbf{x}_A, \mathbf{x}, -t) * \bar{G}^{p,q}(\mathbf{x}_B, \mathbf{x}, t) d^2\mathbf{x}. \tag{22}$$

The predicted output differs, depending on whether the entire surface integral is evaluated (equation (20)) or the near-offset part (with respect to the receiver position where a source is retrieved) is left out (equation (21)). In this section, the correlation integral is numerically tested on the synthesized global responses. The results of the numerical illustration are shown and discussed.

The finite difference-modelled responses (section 3) can be written as a Green's function convolved with a source wavelet. For compactness reasons we leave out this convolution with the source wavelet. Using the Green's function notation, we modeled responses $G^{\nu,p}(\mathbf{x}, \mathbf{x}_A, t)$, $\bar{G}^{p,q}(\mathbf{x}, \mathbf{x}_B, t)$, $G^{p,p}(\mathbf{x}, \mathbf{x}_A, t)$ and $\bar{G}^{\nu,q}(\mathbf{x}, \mathbf{x}_B, t)$. By applying the acoustic source-receiver reciprocity relations, equations (A14)–(A17), but without rotation, we have implicitly also modeled the responses $G^{\nu,p}(\mathbf{x}_A, \mathbf{x}, t)$, $\bar{G}^{p,q}(\mathbf{x}_B, \mathbf{x}, t)$, $G^{\nu,q}(\mathbf{x}_A, \mathbf{x}, t)$ and $-\bar{G}^{p,f}(\mathbf{x}_B, \mathbf{x}, t)$.

Thus we have all the responses needed to illustrate the basic seismic interferometry relation, equation (20).

For testing equation (21), the complete finite difference-modelled responses are not used but rather the Green's functions without the contributions of sources nearby $\mathbf{x}_A$ and $\mathbf{x}_B$.

The seismic interferometry relations only contain a correlation of Green's functions. Our synthesized data are Green's functions convolved with a source wavelet, $s(t)$. Including the source wavelets in the basic seismic interferometry relation in the frequency domain, results in multiplying each term with:

$$\hat{s}^*(\omega)\hat{s}(\omega) = |\hat{s}(\omega)|^2, \tag{23}$$

which is the power spectrum of the source wavelet. In the time domain each term is convolved with

$$s(-t) * s(t), \tag{24}$$

which is the autocorrelation of the source wavelet. Since the finite difference-modelled result is a Green's function convolved with the source wavelet, we correlate it further with the source wavelet to provide it with the same phase information as the reconstructed result. Whenever we speak about the finite difference-modelled Green's function in this section, we mean the finite difference-modelled Green's function correlated with the source wavelet.

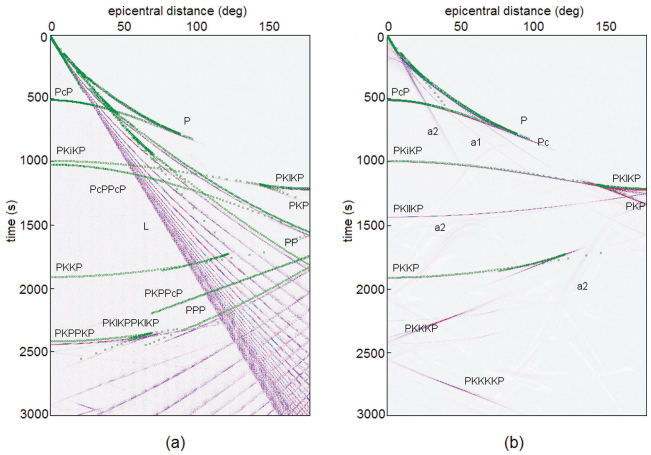

Figure 6 Comparison between finite difference-modelled responses and ray-tracing arrival-time functions. The horizontal axis shows epicentral distance in degrees and the vertical axis shows the time in seconds. The finite difference-modelled reflection responses of the Earth with (a) and without (b) free surface multiples. Ray-tracing arrival times are plotted with green crosses in the same figures. Note that for the finite difference modelling an adjusted version of the PREM model is used (Fig. 4b) whereas for the ray tracing the original PREM model is used (Fig. 4a). Note also that the positive time axis points downwards, as is conventional in exploration-scale seismology but unconventional in solid Earth seismology.

The first step of evaluating equation (22) numerically is a cross-correlation between the v-response measured at $\mathbf{x}_A$, with the p-response without free surface multiples measured at $\mathbf{x}_B$. The correlation of responses with $\mathbf{x}_A$ at 0° Δ and $\mathbf{x}_B$ at $-90^\circ\Delta$ is depicted on the left-hand side of Fig. 7. The horizontal axes represent the source positions, ranging from $\Delta = -180^\circ$ to $\Delta = 180^\circ$ The result on the right-hand side of Fig. 7, is a correlation panel. Each trace in the correlation panel corresponds to a correlation of responses due to the same source.

The second step is visualized in Fig. 8. It is an integration over all the source positions, which in the numerical case is a stack of all traces in the correlation panel. As explained by Schuster *et al.* (2004), Wapenaar *et al.* (2004) and Snieder (2004) events with stationary phases (events that contain a $\partial_x\phi = 0$, where ϕ is the phase of an event and ∂_x denotes the derivative with respect to the source position) in the correlation panel add up during the integration process. All the other amplitudes in the correlation panel cancel by destructive

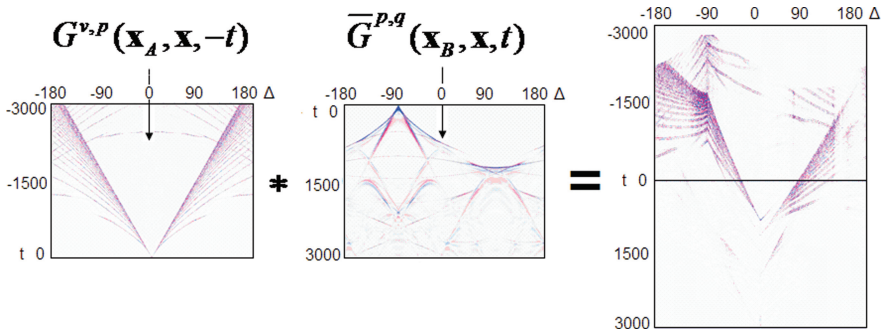

Figure 7 Visualization of the integrand of equation (22). The left panel depicts the time-reversed response of state A recorded at $\Delta = 0^\circ$, for sources in the range $-180^\circ < \Delta < 180^\circ$. It is convolved with the response of state B recorded at -90° epicentral distance (middle panel). The right-hand panel shows the resulting correlation panel.

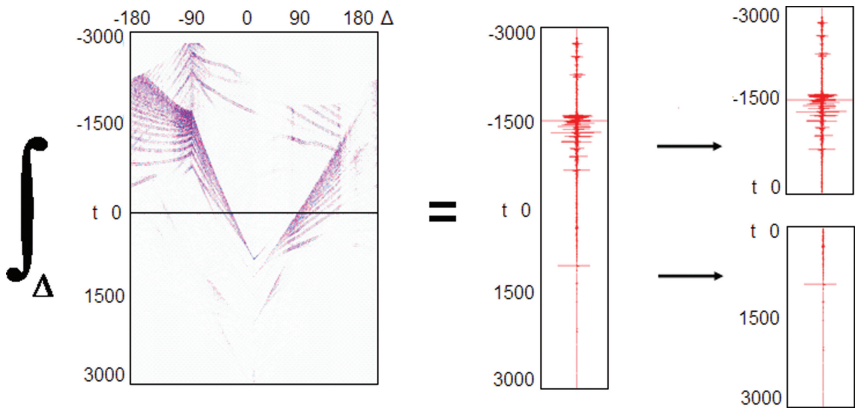

Figure 8 Visualization of the integration process. The traces in the correlation panel (left) are summed to produce the trace in the middle panel. On the right, the causal and anti-causal part are depicted separately.

interference. The resulting single trace (middle panel in Fig. 8) has a causal as well as an anti-causal part. According to equation (20) they should be $G^{v,q}(\mathbf{x}_A, \mathbf{x}_B, -t)$ and $\bar{G}^{p,f}(\mathbf{x}_B, \mathbf{x}_A, t)$, respectively.

Figures 9(a) and 9(b) show the reconstructed time-reversed anticausal Green's function without using near-offset responses for a time duration of 3000 and 6000 s, respectively, according to equation (21). The same amplitude scaling is used for both Figs 9(a) and 9(b). Comparing Fig. 9(a) with Fig. 9(b) it can be seen that until 2000 s the same events are reconstructed and with the same amplitude. At later times, though, we can see in Fig. 9(b) events which cannot be seen in Fig. 9(a). To reconstruct a primary we need at least a first order multiple in the input data (unless there is a delta pulse at time zero in the data). Because the response without free surface multiples contains all the significant events before 2000 s (Fig. 6b), an input duration of 3000 + 2000 s must be sufficient to reconstruct correctly events occurring before 3000 s.

We have shown that by correlating G with $\bar{G}$ stable amplitudes can be retrieved, independent of the duration of the input responses. In the following, we will use an input duration of 6000 s to reconstruct all events before 3000 s with the correct (relative) amplitude.

Continuing our numerical illustration, the described steps of correlation and integration (Figs 7 and 8) are repeated for all $\mathbf{x}_B$'s around the model. That is, the same response $G^{v,p}(\mathbf{x}_A, \mathbf{x}, t)$ is correlated with $\bar{G}^{p,q}(\mathbf{x}_B, \mathbf{x}, t)$ and subsequently integrated, for varying $\mathbf{x}_B$. By doing so we reconstruct responses measured at all epicentral distances, for a source at $\mathbf{x}_A$.

Figures 10(a) and (b) are the first 3000 s of the time-reversed anticausal reconstructed results for, respectively, the seismic interferometry relation, equation (20) and the seismic interferometry relation without near offset, equation (21). The reconstructed results are compared with the expected result, $G^{v,q}(\mathbf{x}_A, \mathbf{x}_B, t)$ as shown in Fig. 10(c). This result was obtained by the direct modelling of a response at $\mathbf{x}_A$ due to sources all around the Earth model.

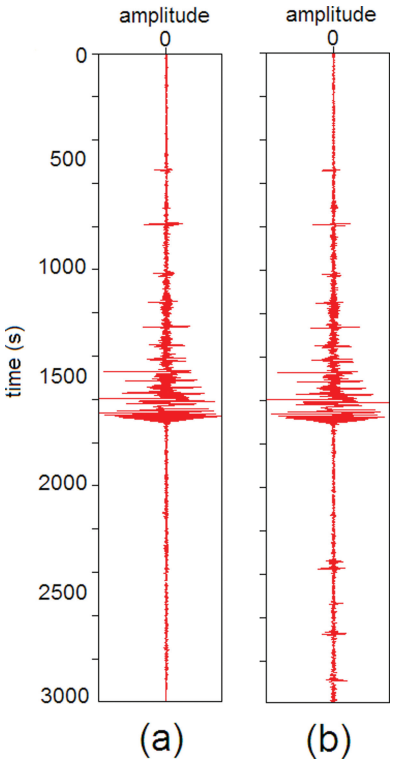

Figure 9 Reconstructed time-reversed anticausal results without using near-offset responses. (a) and (b) are reconstructed traces for $\mathbf{x}_A$ at $\Delta = 90^\circ$ from $\mathbf{x}_B$, using an input response duration of respectively 3000 s and 6000 s.

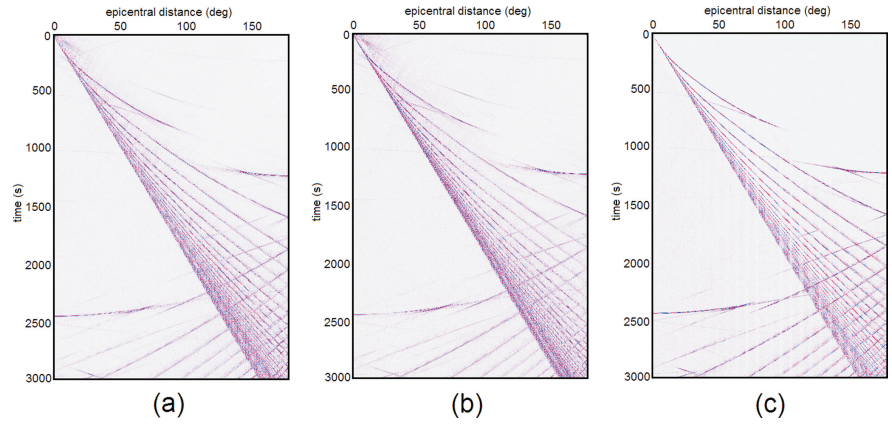

Figure 10 Comparison of the time-reversed anticausal reconstructed result (a) and the reconstruction without using near-offset responses (b) with the finite difference-modelled response (c), which is $G^{v,q}(\mathbf{x}_A, \mathbf{x}, t)$. The horizontal axes show epicentral distance in degrees and the vertical axes show time in seconds. As the responses are axi-symmetric, only the first 180° are shown. One degree Δ corresponds to 8 traces.

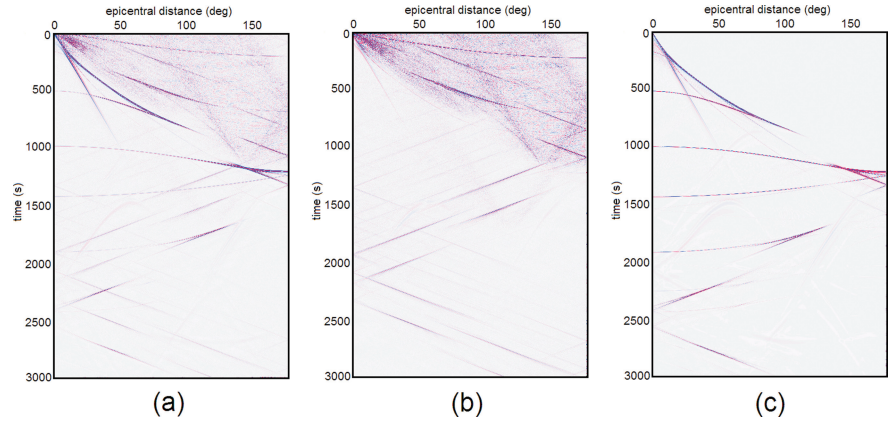

Figure 11 The causal reconstructed result (a), the reconstructed result without using near-offset responses (b) and the finite difference-modelled response (c), which is $\bar{G}^{p,f}(\mathbf{x}, \mathbf{x}_A, t)$. The horizontal axes show epicentral distance in degrees and the vertical axes show time in seconds. For the responses that are axi-symmetric, only the first 180° are shown. One degree Δ corresponds with 8 traces.

There is a very good agreement between the different panels. All the finite difference-modelled events in Fig. 10(c) are reconstructed with seismic interferometry in both Figs 10(a) and 10(b). In (a) and (b) we see, additionally, some noise in the upper left corners and between 50 and 150°Δ. At around 500 s, an event can be noticed, which is not modelled in Fig. 10(c).

Figures 11(a) and (b) are the first 3000 s of the causal reconstructed results for, respectively, the seismic interferometry relation, equation (20) and the seismic interferometry relation without near offset, equation (21), respectively. Figure 11(c) shows the expected causal outcome for equation (20), which is $\bar{G}^{p,f}(\mathbf{x}_B, \mathbf{x}_A, t)$. The expected causal outcome for equation (21) is zero.

At first sight, there is quite a good agreement between the reconstructed responses – Fig. 11(a) and the finite difference-modelled response – Fig. 11(c). After a closer look at Fig. 11(a) it can be seen that all events in Fig. 11(c) have been reconstructed. However, there are strong artefacts as well. We see – especially at earlier times – a noisy signal and before the first 'real' arrival a few events were reconstructed that can not be seen in Fig. 11(c).

Figure 11(b) contains the same artefacts that can be seen in Fig. 11(a). However, as expected, it is an empty response but for the artefacts.

In Appendix B, it is shown that the artefacts in Figs 10 and 11 are due to correlation noise and the reconstruction of internal events. It is shown that in our modelling these are present due to numerical errors. When applying seismic interferometry to actual data, the artefacts could appear due to undersampling of source positions and an unequal illumination of the medium of interest from different angles, respectively.

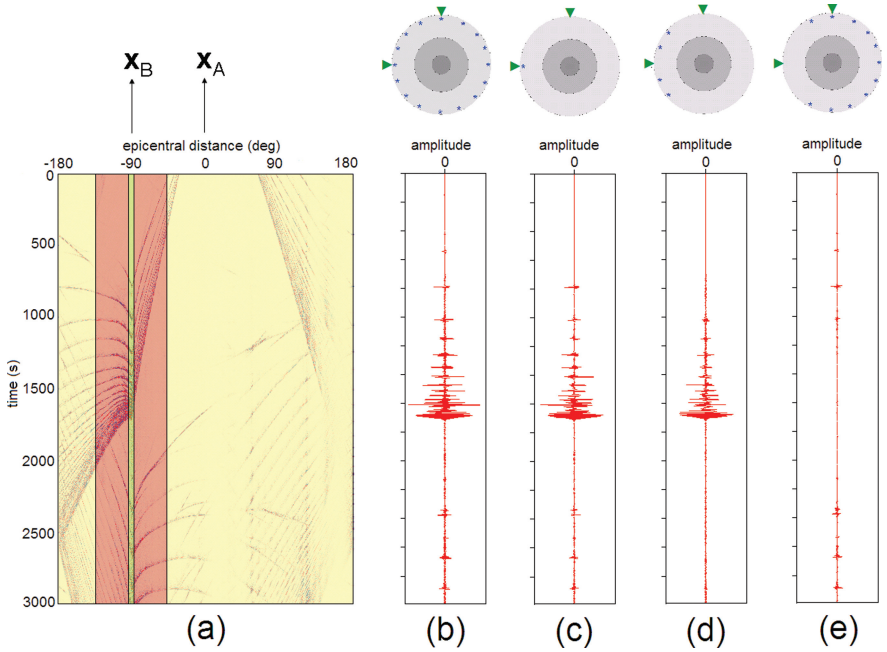

Figure 12 The time-reversed anticausal correlation panel (a) after correlating a response measured at $\mathbf{x}_A$ (at $\Delta = 0°$) with the response without free surface multiples measured at $\mathbf{x}_B(\Delta = -90°)$. The green, red and yellow colours on the correlation panel denote, respectively, the near-offset, mid-offset and far-offset regions (with respect to the location $\mathbf{x}_B$ where we want to retrieve a source). Stacking over the complete correlation panel, the near-offset, mid-offset and far-offset regions, give the traces (b), (c), (d) and (e), respectively. The traces are plotted with the same amplitude scale. The blue stars in the models above the traces indicate source regions from which the responses are observed and used for the reconstruction of the different traces. The green triangles indicate the positions where the responses are measured and between which a response is reconstructed.

We draw the conclusion that by applying equation (20), we have indeed reconstructed $G^{v,q}(\mathbf{x}_A, \mathbf{x}_B, t)$ and $\bar{G}^{p,f}(\mathbf{x}_B, \mathbf{x}_A, t)$. Also without using the near-offset contribution we were able to make a kinematically good estimation of $G^{v,q}(\mathbf{x}_A, \mathbf{x}_B, t)$ but not of $\bar{G}^{p,f}(\mathbf{x}_B, \mathbf{x}_A, t)$, as was expected by equation (21). The artefacts can be explained by numerical errors.

We evaluated the relations on a lossless Earth, since in our derivations no losses were assumed. Roux *et al.* (2005) and Slob *et al.* (2006) showed that when seismic interferometry is applied for media with moderate losses, still correct traveltimes but approximate amplitudes are retrieved. Internal events (Appendix B) are amplified as soon as losses are introduced.

5. TOWARDS APPLICATION

Thus far, we have considered ideal or semi-ideal situations with the availability of sources all around the globe or missing only near-offset sources. In reality, we will not have a dense (earthquake) source distribution in some mid- and far-offsets either. In this section, we show by stationary phase analysis that also under suboptimal conditions we can still retrieve useful information from the application of the global-scale seismic interferometry relations.

5.1. Stationary phase localization

The working principle of seismic interferometry can be described as follows. First, observed responses measured at different epicentral distances and due to the same sources, are correlated. Therewith, higher-order events become lower-order events. At times belonging to the kinematics of the Green's function that would be observed between the two locations between which the responses are measured, stationary phase events appear in the correlation panel. Then by stacking over the correlation panel, the signals at the stationary phases are selected and thus the desired Green's function is reconstructed. With a stationary phase event we mean a (part of an) event which contains a stationary phase. In this section, we analyse where these stationary phase events are located in the anticausal correlation panels.

In Fig. 12(a) we show the same anticausal part of the correlation panel as in Fig. 7, which was the result after correlating a response measured at $0°\Delta$ with the multiple-free

response measured at $-90^\circ\Delta$, both due to the same sources at all epicentral distances. To build up the correlation panel, 5760 sources around the model were used to satisfy the Nyquist spatial sampling criterion (Appendix B). In Fig. 12(a) the different regions of this correlation panel are indicated by colours. The near-offset region, the region with correlations of responses due to sources that are close to the location $\mathbf{x}_B$ where we want to retrieve a source, is indicated by green. The mid- (red) and far-offset (yellow) regions are the correlations of responses due to sources that are at an intermediate to far epicentral distance with respect to the location $\mathbf{x}_B$ where we want to retrieve a source.

The locations of the stationary phase events can be recognized in the correlation panel (Fig. 12a) by noticing pieces of events where $\partial_x\phi = 0$. We subsequently stack over the different offset regions to identify the locations of the stationary phase events that we might not directly identify visually on the correlation panel. The resulting traces are in Figs 12(b)–(e). With the blue stars on the Earth models above the traces it is indicated from what epicentral distances the responses were used during the stacking.

When we stack over the complete correlation panel we obtain trace Fig. 12(b). When we only stack over the near-offset region, we obtain trace Fig. 12(c). It looks similar to Fig. 12(b). The near offset (in fact the zero offset) contains all the reconstructed events. When we stack over the mid-offset region we catch stationary phase events. The stacking result is trace Fig. 12(d). The far-offset region in the correlation panel contains stationary phase events for constructing events at later times and additional events, as can be seen in the resulting trace Fig. 12(e).

These observations match with the theory as expressed in equations (20) and (21). Practically, this means that to reconstruct certain events (kinematically correct), we only need to have the part of the (anticausal) correlation panel where the stationary phase arrivals occur. Thus to reconstruct a certain event, we only need responses from sources from a certain range of epicentral distances. In the next section, we clarify the possibilities of applying an seismic interferometry relation, equation (21), on global-scale seismological data by means of an example.

5.2. PcP retrieval

Assume we want to retrieve information about the core-mantle boundary at the question mark location in Fig. 13. We have seismic stations at locations $\mathbf{x}_A$ and $\mathbf{x}_B$, at $\Delta = 0^\circ$ and 45° on either side of the core-mantle boundary part of interest.

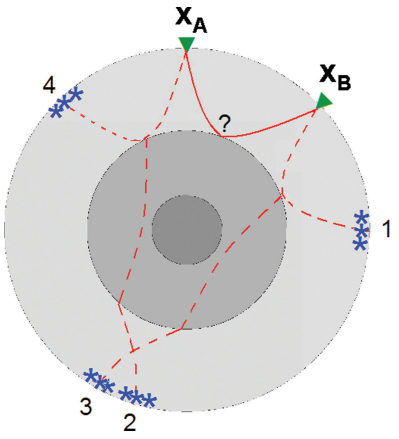

Figure 13 Possible contributions for retrieving PcP between $\mathbf{x}_A$ at $\Delta = 0^\circ$ and $\mathbf{x}_B$ at 45°. 1, 2, 3 and 4 denote seismically active regions at around $\Delta = 90$, -165°, -150° and -45° from $\mathbf{x}_A$, respectively.

However, since the Earth is not seismically active near $\mathbf{x}_A$ and $\mathbf{x}_B$, we cannot directly measure PcP between $\mathbf{x}_A$ and $\mathbf{x}_B$. There are 4 obvious possibilities in which we can still retrieve PcP by using seismic interferometry (sources in region 1, 2, 3 or 4 in Fig. 13). Assume the Earth is seismically active at around $\Delta = -45^\circ$ (region 4) or at around 90° (region 1), then we can correlate PcPPcP with PcP or *vice versa* to retrieve PcP. If the Earth is seismically active at around -150° (region 3) or at around -165° (region 2), then we can correlate PKP with PKPPcP or vice versa to retrieve PcP. The epicentral distance values are not exact and only valid for our simplified Earth model (Fig. 4b). In our modeling, PKPPcP is a clearer arrival than PcPPcP (Fig. 6). Thus here we use sources at around -150° (region 3 in Fig. 13) to retrieve PcP.

Figure 14(a) is a small portion of the correlation panel for $\mathbf{x}_A$ and $\mathbf{x}_B$ at 0° and 45° and sources between -165° and -135°. The horizontal axis depicts the locations of the sources. The stationary phase for PcP due to a correlation of PKPPcP (state *A*) with PKP (state *B*) can be distinguished between -160° and -140°, around 610 s. Figure 14(b) is simply the contribution from the source right at the stationary phase ($\Delta = -148^\circ$). Since with our modelling we know the exact location of the stationary phase, the contribution from just one source already suffices to retrieve PcP, although we would need to time-window the trace around the estimated PcP arrival time between $\mathbf{x}_A$ and $\mathbf{x}_B$, since at other times we have correlation noise. In reality, because of unknown deviations from a 1D reference model, we would need to stack over contributions from sources at an estimated range in which the stationary phase could be located. Figure 14(c) is a stack of all the source contributions between -160° and -140°, as

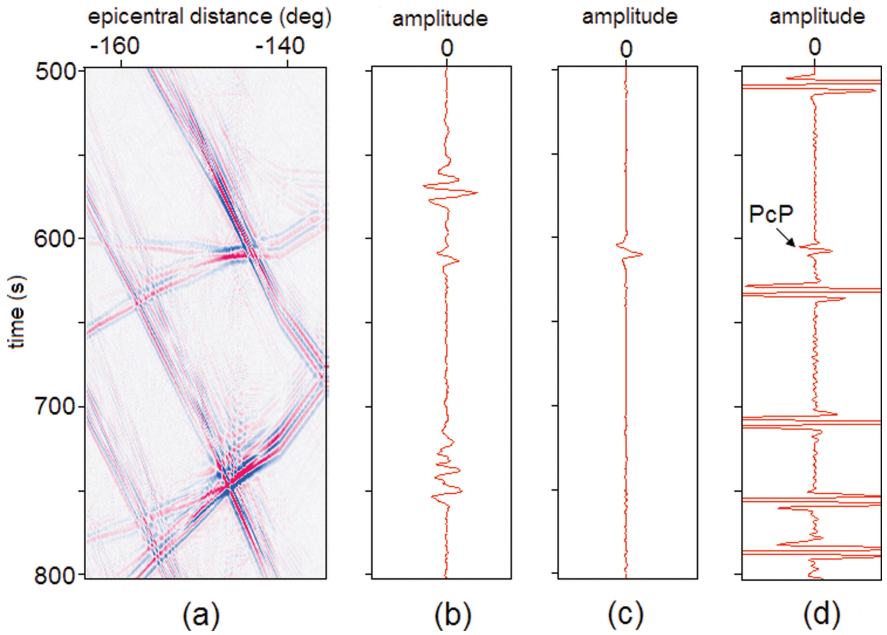

Figure 14 PcP retrieval between $\mathbf{x}_A$ and $\mathbf{x}_B$ at $\Delta = 45°$. (a) Portion of time-reversed anticausal correlation panel including the stationary phase for retrieval of PcP. (b) Trace at $\Delta = -148°$ from the correlation panel. (c) Summation of (a) over source positions. (d) Finite difference-modelled response between $\mathbf{x}_A$ and $\mathbf{x}_B$.

plotted in Fig. 14(a). Because of an ideal sampling (1 source per 7 km), just PcP is now retrieved and (almost) all correlation noise disappears. Figure 14(d) is the directly finite difference-modelled response between $\mathbf{x}_A$ and $\mathbf{x}_B$. Comparing Fig. 14(c) with Fig. 14(d) we see that the kinematic retrieval of PcP is exact but there are (numerical) errors in the phase characteristics.

In reality, we might not have available the responses due to dense source distributions around one of the four regions in Fig. 13. We can still retrieve reflection information of the question mark location on the core-mantle boundary in Fig. 13, however, if we have an array of receivers at location $\mathbf{x}_A$ and or $\mathbf{x}_B$ and combine seismic interferometry with migration. With an integration over receiver positions, as imbedded in the migration, the stationary phase contribution can be captured that would otherwise be missed by having only the response from one source in one of the four regions (Schuster *et al*. 2004; Wapenaar *et al*. 2004; Artman *et al*. 2004; Draganov *et al*. 2004a).

The source sampling around the globe is very good along specific lines, the lithospheric plate boundaries (Fig. 1) but not over large areas. Therefore, it is most practical to use receivers that are in line with major earthquake belts and to apply seismic interferometry in an approximate 2D sense, as in the above example. For a retrieved elastodynamic response, subsequently, another interferometric step can be used to isolate the surface waves (Halliday *et al*. 2007).

As input for our seismic interferometry algorithms we need one response with and one without free surface multiples. It is not easy to find a response with all the free surface multiples removed, whereas all the other events are undistorted. E.g., a data driven method like surface related multiple removal (SRME) could be used. With the current sampling of sources and receivers on a global scale though, it is not yet feasible. As shown in this section, seismic interferometry can still be applied. In the above example the response without free surface multiples is easily found by time windowing the response measured at $\mathbf{x}_B$ around the time that PKP is expected. A similar approach is taken in Bakulin *et al*. (2007). Another possibility would be to use wavefield separation to approximate a response without free surface multiples (Mehta *et al*. 2007) or we could use the response including free surface multiples but due to sources at varying depths. With this approach Draganov *et al*. (2006) removed ghost events due to reflectors below the sources.

5.3. Removing undesired events

Because we know already roughly the velocity and density model of the Earth, we can model in what region of the

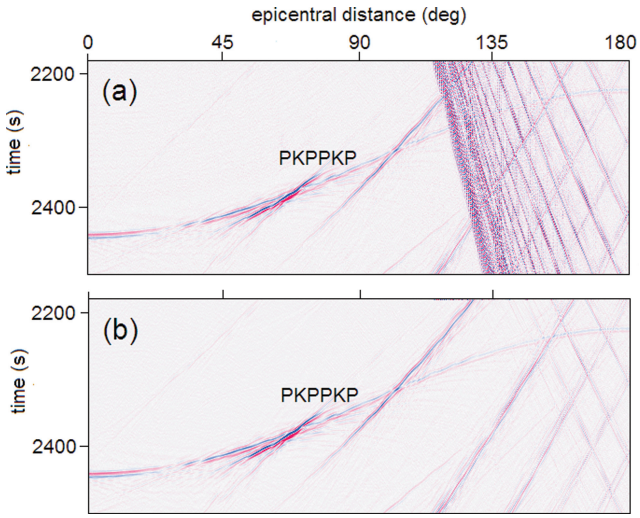

Figure 15 Comparison of time-reversed anticausal reconstructions. For the upper panel, responses from sources all around the model (except the near offset) were used. For the lower panel, the responses from sources between $\Delta = -24^\circ$ and 24° were omitted.

correlation panels stationary phase events are expected. We can use this knowledge to select these events and to omit stationary phase events leading to the reconstruction of undesired events. In this subsection, we illustrate this by trying not to reconstruct the very high-order free surface multiples.

From an analysis as in Fig. 12, we know that the stationary phase events of the high-order free surface multiples occur in the near-offset and a part of the mid-offset region of the correlation panels. Figure 15(a) is a portion of Fig. 10, the time-reversed anticausal reconstruction result. Beyond $\Delta = 100^\circ$ a dense set of free surface multiples obscures the PKPPKP event. We repeat the same application of seismic interferometry that was used to retrieve the response in Fig. 15(a), but now omitting the responses from sources between $\Delta = -24^\circ$ and 24°). Figure 15(b) is a portion of the result. It indeed does not contain a large part of the higher-order free surface multiples, whereas event PKPPKP is preserved. Where PKPPKP was masked by free surface multiples in Fig. 15(a) it can clearly be seen in Fig. 15(b). We can achieve this result because stationary phase events leading to events that overlap in the reconstructed result do not generally overlap in the correlation panel. Hence, the correlation panel can effectively be used as a domain to filter out (un)desired events.

6. CONCLUSIONS

We derived elastodynamic seismic interferometry relations for transient sources near the closed surface of the Earth. This configuration intrinsically differs from configurations in which seismic interferometry has been applied to thus far. The derived relations consist in a correlation integral, in which a response with free surface multiples at one receiver is correlated with a response without free surface multiples at another. A response without free surface multiples is necessary to prevent the occurrence of ghost events and to allow stable amplitude reconstructions in a closed system. Subsequently, the correlation result is integrated over the source locations, thus reconstructing a response between the two receiver locations.

The rotation of the Earth breaks source-receiver reciprocity but seismic interferometry relations are still valid. No extra term needs to be evaluated to take the Coriolis force into account.

Using synthesized global-scale earthquake responses we illustrated the acoustic versions of the derived seismic interferometry relation for a non-rotating Earth. We also tested a slightly different seismic interferometry relation for the situation when no near-offset responses are available. Both relations gave the expected reconstructed results. When responses due to sources all around the Earth, are available both the full Green's function and the Green's function without free surface multiples is reconstructed. When no responses are available from sources nearby the receiver position where we want to reconstruct a source, only the Green's function including the free surface multiples can be reconstructed.

The reconstructions were not without artefacts, namely, noise and additional events. We showed that these artefacts could be explained to be due to numerical errors.

For applications to global seismology, only the seismic interferometry relation without near offset will be of use. Given the distribution of earthquakes around the globe, it will not be possible to reconstruct the complete response between any two receiver positions, since an overall dense source sampling is required. We showed that with a dense source sampling at a specific range of epicentral distances, we can still retrieve specific events between receiver positions. If the location of a stationary phase is known or if an array of receivers is used, one good quality earthquake response could suffice to retrieve an event between receiver positions.

For the application of seismic interferometry to actual earthquake data, preprocessing would be necessary. Responses due to different sources would need to be deconvolved for the different source wavelets, normalized for the differences in magnitude and filtered for the differences in source directivity. Free surface multiples would need to be separated. Also, because in the derivation of seismic interferometry lossless media

are assumed, factors need to be included that account for anelastic losses.

Since the approximate velocity and density model of the Earth is already known, we can find out by modelling where in the correlation panel the stationary phases of specific events occur. Subsequently, we can determine whether we properly sample certain stationary phase events with a (given) source-receiver configuration. Hence, we have a tool to estimate what kind of events in the Green's function between two points on the surface can be reconstructed, given responses from a certain range of epicentral distances with sources. We demonstrated that this knowledge of stationary phase locations in the correlation panel can also be used to filter out undesired events.

ACKNOWLEDGEMENTS

This research is supported by The Netherlands Research Centre for Integrated Solid Earth Sciences (ISES) and The Netherlands Organisation for Scientific Research (NWO). The authors would like to thank Xander Campman, Evert Slob, Jeannot Trampert and Arie Verdel for insightful comments, Jan Thorbecke for support in implementing the finite difference modelling, Andrey Bakulin and Roel Snieder for careful reviews and we would also like to thank Roel Snieder for his inspiration to extend the theory for rotating media. We used software from the Delphi and CWP consortium.

REFERENCES

Abe S., Kurashimo E., Sato H., Hirata N., Iwasaki T. and Kawanaka T. 2007. Interferometric seismic imaging of crustal structure using scattered teleseismic waves. *Geophysical Research Letters* **34**, L19305.

Artman B., Draganov D., Wapenaar K. and Biondi B. 2004. Direct migration of passive seismic data, 66th EAGE meeting, Paris, France, Extended Abstracts, P075.

Bakulin A. and Calvert R. 2004. Virtual Source: new method for imaging and 4D below complex overburden, 74th SEG meeting, Denver, Colorado, USA, Expanded Abstracts, 2477–2480.

Bakulin A., Mateeva A., Calvert R., Jorgensen P. and Lopez, J. 2007. Virtual shear source makes shear waves with air guns. *Geophysics* **72**, A7–A11.

Berkhout A.J. and Verschuur D.J. 1997. Estimation of multiple scattering by iterative inversion, Part I: Theoretical considerations. *Geophysics* **62**, 1586–1595.

Campillo M. and Paul A. 2003. Long-range correlations in the diffuse seismic coda. *Science* **299**, 547–549.

Claerbout J.F. 1968. Synthesis of a layered medium from its acoustic transmission response. *Geophysics* **33**, 264–269.

Dahlen F.A. and Tromp J. 1998. *Theoretical Global Seismology*. Princeton University Press, Princeton, New Jersey.

de Hoop A.T. 1988. Time-domain reciprocity theorems for acoustic wave fields in fluids with relaxation. *Journal of the Acoustic Society of America* **84**, 1877–1882.

Derode A., Larose E., Tanter M., de Rosny J., Tourin A., Campillo M. and Fink M. 2003. Recovering the Green's function from field-field correlations in an open scattering medium. *Journal of the Acoustic Society of America* **113**, 2973–2976.

Draganov D., Wapenaar K., Artman B. and Biondi B. 2004. Migration methods for passive seismic data. 74th SEG meeting, Denver, Colorado, USA, Expanded Abstracts, ST 1.5.

Draganov D., Wapenaar K. and Thorbecke J. 2004. Passive seismic imaging in the presence of white noise sources. *The Leading Edge* **23**, 889–892.

Draganov D., Wapenaar K. and Thorbecke, J. 2006. Seismic interferometry: Reconstructing the earth's reflection response. *Geophysics* **71**, SI61–SI70.

Draganov D., Wapenaar K., Mulder W., Singer J. and Verdel A. 2007. Retrieval of reflections from seismic background-noise measurements. *Geophysical Research Letters* **34**, L04305.

Dziewonski M. and Anderson D.L. 1981. Preliminary reference earth model, *Physics of The Earth and Planetary Interiors* **25**, 297–356.

Fan C., Pavlis G.L., Weglein A.B. and Nita B.G. 2006. Removing free-surface multiples from teleseismic transmission and constructed reflection responses using reciprocity and the inverse scattering series. *Geophysics* **71**, SI71–SI78.

Fokkema J.T. and van den Berg P.M. 1993. *Seismic Applications of Acoustic Reciprocity*. Elsevier.

Gerstoft P., Sabra K.G., Roux P., Kuperman W.A. and Fehler M.C. 2006. Green's functions extraction and surface-wave tomography from microseisms in Southern California. *Geophysics* **71**, S123–S131.

Halliday D.F., Curtis A., Robertsson J.O.A. and van Manen D.J. 2007. Interferometric surface-wave isolation and removal. *Geophysics* **72**, A69–A73.

Knapmeyer M. 2004. TTBox: A Matlab toolbox for the computation of 1D teleseismic travel times. *Seismological Research Letters* **75**, 726–733.

Kumar M.R. and Bostock M.G. 2006. Transmission to reflection transformation of teleseismic wavefields. *Journal of Geophysical Research* **111**, B08306.

Levander A. 2003. USArray design implications for wavefield imaging in the lithosphere and upper mantle. *The Leading Edge* **22**, 250–255.

Lines L. R., Slawinski R. and Bording R.P. 1999. A recipe for stability of finite-difference wave-equation computations. *Geophysics* **64**, 967–969.

Mehta K., Bakulin A., Sheiman J., Calvert R. and Snieder R. 2007. Improving the virtual source method by wavefield seperation. *Geophysics* **72**, V79–V86.

Pao Y.H. and Varatharajulu V. 1976. Huygens' principle, radiation conditions, and integral formulations for the scattering of elastic waves. *Journal of the Acoustic Society of America* **59**, 1361–1371.

Roux P. and Fink M. 1997. Experimental evidence in acoustics of the violation of time reversal invariance induced by vorticity. *Europhysics Letters* **32**, 25–29.

Roux P., Sabra K.G., Kuperman W.A. and Roux A. 2005. Ambient noise cross correlation in free space: Theoretical approach. *Journal of the Acoustic Society of America* **117**, 79–84.

Schuster G.T. 2001. Theory of daylight/interferometric imaging: tutorial. 63rd EAGE meeting, Amsterdam, The Netherlands, Extended Abstracts, A-32.

Schuster G.T., Yu J., Sheng J. and Rickett J. 2004. Interferometric/daylight seismic imaging. *Geophysical Journal International* **157**, 838–852.

Shapiro N.M., Campillo M., Stehly L. and Ritzwoller M.H. 2005. High-resolution surface wave tomography from ambient seismic noise. *Science* **307**, 1615–1618.

Shiraishi K., Onishi K., Ito S., Aizawa T. and Matsuoka T. 2006. Seismic interferometry with underground moving source. 68th EAGE meeting, Vienna, Austria, Expanded Abstracts, A043.

Shragge J., Artman B. and Wilson C. 2006. Teleseismic shot-profile migration. *Geophysics* **71**, SI221–SI229.

Slob E., Draganov D. and Wapenaar K. 2006. GPR without a source. *Proceedings of the Eleventh International Conference on Ground Penetrating Radar*, (Ohio State University, Columbus, OH.

Snieder R. 2004. Extracting the Green's function from the correlation of coda waves: a derivation based on stationary phase. *Physical Review E* **69**, 046610-1–046610-8.

Snieder R. 2007. Extracting the Green's function of attenuating acoustic media from uncorrelated waves. *Journal of the Acoustic Society of America* **121**(5), 2637–2643.

Storchak D.A., Schweitzer J. and Bormann P. 2003. The IASPEI standard seismic phase list. *Seismological Research Letters* **74**, 761–772.

Verschuur D.J. and Berkhout A.J. 1997. Estimation of multiple scattering by iterative inversion, Part II: Practical aspects and examples. *Geophysics* **62**, 1596–1611.

Virieux J. 1986. P-SV wave propagation in heterogeneous media: Velocity-stress finite-difference method. *Geophysics* **51**, 889–901.

Wapenaar K. 2006. Nonreciprocal Green's function retrieval by cross correlation. *Journal of the Acoustic Society of America* **120**, EL7–EL13.

Wapenaar K. and Fokkema J.T. 2006. Green's functions representations for seismic interferometry. *Geophysics* **71**, SI33–SI46.

Wapenaar K., Thorbecke J.W., Draganov D. and Fokkema J.T. 2002. Theory of acoustic daylight imaging revisited. 72nd SEG meeting, Salt lake Ciry, Utah, USA, Expanded Abstracts, ST 1.5.

Wapenaar K., Draganov D., van der Neut J. and Thorbecke J.W. 2004. Seismic interferometry: a comparison of approaches. 74th SEG meeting, Denver, Colorado, USA, Expanded Abstracts, ST 1.5.

Weaver R.L. and Lobkis O.I. 2001. Ultrasonics without a source: thermal fluctuation correlations at MHz frequencies. *Physical Review Letters* **87**, 134301-1–134301-4.

Yao H., van der Hilst R.D. and de Hoop M.V. 2006. Surface-wave array tomography in SE Tibet from ambient seismic noise and two-station analysis: I - phase velocity maps. *Geophysical Journal International* **166**, 732–744.

APPENDIX A: DERIVATION OF GENERALIZED SOURCE-RECEIVER RECIPROCITY RELATIONS

In this appendix the generalized source-receiver reciprocity relations for Green's functions are derived. Roux and Fink (1997) studied experimentally the violation of acoustic time-reversal for a rotating medium. In Dahlen and Tromp (1998) the general relation between a Green's function in the actual Earth and a Green's function in an Earth with a reversed sense of rotation (the anti-Earth) is given. Here we perform the derivations in order to find the relevant relations for the source and receiver characteristics that are used in this paper.

We start with the Rayleigh-Betti reciprocity theorem of the convolution type:

$$\begin{aligned}\oint_{\partial\mathbb{D}} &\{\hat{v}_{i,A}\hat{\tau}_{ik,B} - \hat{\tau}_{ik,A}\hat{v}_{i,B}\}n_k d^2\mathbf{x}\\ &= \int_{\mathbb{D}} \{-\hat{\tau}_{ij,A}\hat{h}_{ij,B} - \hat{v}_{i,A}\hat{f}_{i,B} + \hat{h}_{ij,A}\hat{\tau}_{ij,B} + \hat{f}_{i,A}\hat{v}_{i,B}\}d^3\mathbf{x}\\ &- \int_{\mathbb{D}} \{2\rho\epsilon_{ijk}\hat{v}_{i,B}\Omega_{j,B}\hat{v}_{k,A} - 2\rho\epsilon_{ijk}\hat{v}_{i,A}\Omega_{j,A}\hat{v}_{k,B}\}d^3\mathbf{x}, \qquad \text{(A1)}\end{aligned}$$

which is found by repeating the derivation for the Rayleigh-Betti reciprocity theorem of the correlation type (section 2.2.1, equation (6)), but by using the interaction function $\{\hat{v}_{i,A}\hat{\tau}_{ij,B} - \hat{\tau}_{ij,A}\hat{v}_{i,B}\}$ instead of $\{-\hat{v}^*_{i,A}\hat{\tau}_{ij,B} - \hat{\tau}^*_{ij,A}\hat{v}_{i,B}\}$, and assuming equal medium parameters in both states.

Using the property $\epsilon_{ijk} = -\epsilon_{kji}$ we may rewrite the integral with the Coriolis terms, the second integral on the right-hand side of equation (A1), as

$$-\int_{\mathbb{D}} \{2\rho\epsilon_{ijk}\hat{v}_{i,B}\Omega_{j,B}\hat{v}_{k,A} + 2\rho\epsilon_{ijk}\hat{v}_{i,B}\Omega_{j,A}\hat{v}_{k,A}\}d^3\mathbf{x}. \qquad \text{(A2)}$$

This integrand will vanish for $\Omega_{j,A} = -\Omega_{j,B}$, i.e., when the medium in state A is rotating opposite to the medium in state B. We choose $\Omega_{j,A} = \Omega_j$, which is a constant angular velocity and $\Omega_{j,B} = -\Omega_j$. Thus the Rayleigh-Betti reciprocity theorem of the convolution type reduces to

$$\begin{aligned}\oint_{\partial\mathbb{D}} &\{\hat{v}_{i,A}\hat{\tau}_{ik,B} - \hat{\tau}_{ik,A}\hat{v}_{i,B}\}n_k d^2\mathbf{x}\\ &= \int_{\mathbb{D}} \{-\hat{\tau}_{ij,A}\hat{h}_{ij,B} - \hat{v}_{i,A}\hat{f}_{i,B} + \hat{h}_{ij,A}\hat{\tau}_{ij,B} + \hat{f}_{i,A}\hat{v}_{i,B}\}d^3\mathbf{x}. \qquad \text{(A3)}\end{aligned}$$

A domain $\mathbb{D}$ enclosed by a surface $\partial\mathbb{D}$ covers the entire inner space of the Earth, hence $\partial\mathbb{D}$ coincides with the free surface (Fig. 16a). Only when sources are represented as boundary conditions at the free surface, the traction vector $\hat{\tau}_{ik}n_k$ at $\partial\mathbb{D}$ will not be equal to zero. By making different choices for the sources in states A and B we end up with the desired relations for interchanging source and receiver positions.

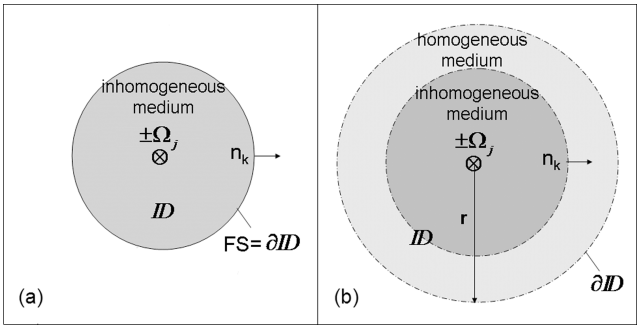

Figure 16 Two configurations for the application of the elastodynamic reciprocity theorem, one with a closed free surface (FS) (a) and one unbounded configuration (b).

Table 3 States for the elastodynamic reciprocity theorem with a traction source in state A and a deformation-rate source in state B.

		State A: free surface	State B: free surface
wavefield	$\hat{\tau}_{ij}$	$\hat{G}^{\tau,\tau}_{ij,p}(\mathbf{x}, \mathbf{x}_A, \omega \mid \mathbf{\Omega})$	$\hat{G}^{\tau,h}_{ij,qr}(\mathbf{x}, \mathbf{x}_B, \omega \mid -\mathbf{\Omega})$
$\mathbf{x} \in \mathbb{D}$	$\hat{v}_i$	$\hat{G}^{v,\tau}_{i,p}(\mathbf{x}, \mathbf{x}_A, \omega \mid \mathbf{\Omega})$	$\hat{G}^{v,h}_{i,qr}(\mathbf{x}, \mathbf{x}_B, \omega \mid -\mathbf{\Omega})$
wavefield	$\hat{\tau}_{ik}n_k$	$\delta(\mathbf{x} - \mathbf{x}_A)\delta_{ip}$	0
$\mathbf{x} \in \partial\mathbb{D}$	$\hat{v}_i$	$\hat{G}^{v,\tau}_{i,p}(\mathbf{x}, \mathbf{x}_A, \omega \mid \mathbf{\Omega})$	$\hat{G}^{v,h}_{i,qr}(\mathbf{x}, \mathbf{x}_B, \omega \mid -\mathbf{\Omega})$
source	$\hat{h}_{ij}$	0	$\delta(\mathbf{x} - \mathbf{x}_B)\delta_{iq}\,\delta_{jr}$
$\mathbf{x} \in \mathbb{D}$	$\hat{f}_i$	0	0

One choice is to represent the source in state A as a boundary condition for the traction at the free surface. In state B a deformation-rate source is chosen within the domain $\mathbb{D}$. The resulting expressions for the source and wavefield states at $\mathbb{D}$ and $\partial\mathbb{D}$ are given in Table 3. Substituting the states of Table 3 into equation (A3), making use of the sifting property of the delta function and the multiplication property of the Kronecker delta function, yields:

$$\hat{G}^{\tau,\tau}_{qr,p}(\mathbf{x}_B, \mathbf{x}_A, \omega \mid \mathbf{\Omega}) = \hat{G}^{v,h}_{p,qr}(\mathbf{x}_A, \mathbf{x}_B, \omega \mid -\mathbf{\Omega}), \tag{A4}$$

in which $\mathbf{\Omega}$ denotes a solid rotation of the medium in $\mathbb{D}$.

Another choice is to represent both the sources in states A and B as boundary conditions for the traction at the free surface. As there are no sources within $\mathbb{D}$ the first integral on the right-hand side of equation (A3) will vanish. Thus, the only term left over from equation (A3) is the surface integral over the wavefield interactions:

$$\oint_{\partial\mathbb{D}} \{\hat{v}_{i,A}\hat{\tau}_{ik,B} - \hat{\tau}_{ik,A}\hat{v}_{i,B}\}n_k d^2\mathbf{x} = 0. \tag{A5}$$

The resulting expressions for the wavefield state at $\partial\mathbb{D}$ are given in Table 4. Substituting the states of Table 4 into equation (A5), making use of the properties of the delta functions and bringing one of the resulting terms to the other side of the equal sign, we obtain

$$\hat{G}^{v,\tau}_{q,p}(\mathbf{x}_B, \mathbf{x}_A, \omega \mid \mathbf{\Omega}) = \hat{G}^{v,\tau}_{p,q}(\mathbf{x}_A, \mathbf{x}_B, \omega \mid -\mathbf{\Omega}). \tag{A6}$$

Next, an Earth without free surface is assumed. As in Fokkema and van den Berg (1993) domain $\mathbb{D}$ is chosen to be unbounded. It consists of two parts, as depicted in Fig. 16(b). The inner part is an inhomogeneous medium and contains the sources. The outer part consists of a source-free homogeneous medium and surrounds the first part.

The surface integral in equation (A3) vanishes on account of the radiation conditions (Pao and Varatharajulu 1976). Thus, the only term left over from equation (A3) is the volume integral over the source-wavefield interactions

$$\int_{\mathbb{D}} \{-\hat{\tau}_{ij,A}\hat{h}_{ij,B} - \hat{v}_{i,A}\hat{f}_{i,B} + \hat{h}_{ij,A}\hat{\tau}_{ij,B} + \hat{f}_{i,A}\hat{v}_{i,B}\}d^3\mathbf{x} = 0. \tag{A7}$$

By making various choices for the sources in states A and B we end up with the desired relations for interchanging source and receiver positions.

One choice is to represent the source in state A as a deformation-rate source, initiating a wavefield at $\mathbf{x}_A$. For state B a force source is chosen, initiating a wave at $\mathbf{x}_B$. The resulting expressions for the source and wavefield states are given in Table 5.

Table 4 States for the elastodynamic reciprocity theorem with traction sources in both states.

		State A: free surface	State B: free surface
wavefield	$\hat{\tau}_{ik}n_k$	$\delta(\mathbf{x} - \mathbf{x}_A)\delta_{ip}$	$\delta(\mathbf{x} - \mathbf{x}_B)\delta_{iq}$
$\mathbf{x}\partial\mathbb{D}$	$\hat{v}_i$	$\hat{G}^{v,\tau}_{i,p}(\mathbf{x}, \mathbf{x}_A, \omega \mid \mathbf{\Omega})$	$\hat{G}^{v,\tau}_{i,q}(\mathbf{x}, \mathbf{x}_B, \omega \mid -\mathbf{\Omega})$

Table 5 States for the elastodynamic reciprocity theorem with a deformation-rate source in state A and a force source in state B.

		State A: no free surface	State B: no free surface
wavefield	$\hat{\tau}_{ij}$	$\hat{\tilde{G}}^{\tau,h}_{ij,pr}(\mathbf{x}, \mathbf{x}_A, \omega \mid \mathbf{\Omega})$	$\hat{\tilde{G}}^{\tau,f}_{ij,q}(\mathbf{x}, \mathbf{x}_B, \omega \mid -\mathbf{\Omega})$
$\mathbf{x} \in \mathbb{D}$	$\hat{v}_i$	$\hat{\tilde{G}}^{v,h}_{i,pr}(\mathbf{x}, \mathbf{x}_A, \omega \mid \mathbf{\Omega})$	$\hat{\tilde{G}}^{v,f}_{i,q}(\mathbf{x}, \mathbf{x}_B, \omega \mid -\mathbf{\Omega})$
source	$\hat{h}_{ij}$	$\delta(\mathbf{x} - \mathbf{x}_A)\delta_{ip}\,\delta_{jr}$	0
$\mathbf{x} \in \mathbb{D}$	$\hat{f}_i$	0	$\delta(\mathbf{x} - \mathbf{x}_B)\delta_{iq}$

Table 6 States for the elastodynamic reciprocity theorem with deformation-rate sources in both states.

		State *A*: no free surface	State *B*: no free surface
wavefield	$\hat{\tau}_{ij}$	$\hat{\bar{G}}^{\tau,h}_{ij,pr}(\mathbf{x},\mathbf{x}_A,\omega \mid \mathbf{\Omega})$	$\hat{\bar{G}}^{\tau,h}_{ij,qs}(\mathbf{x},\mathbf{x}_B,\omega \mid -\mathbf{\Omega})$
$\mathbf{x}\in\mathbb{D}$	$\hat{v}_i$	$\hat{\bar{G}}^{v,h}_{i,pr}(\mathbf{x},\mathbf{x}_A,\omega \mid \mathbf{\Omega})$	$\hat{\bar{G}}^{v,h}_{i,qs}(\mathbf{x},\mathbf{x}_B,\omega \mid -\mathbf{\Omega})$
source	$\hat{h}_{ij}$	$\delta(\mathbf{x}-\mathbf{x}_A)\delta_{ip}\ \delta_{jr}$	$\delta(\mathbf{x}-\mathbf{x}_B)\delta_{iq}\ \delta_{js}$
$\mathbf{x}\in\mathbb{D}$	$\hat{f}_i$	0	0

Substituting the states of Table 5 into equation (A7) and making use of the properties of the delta functions, yields:

$$\hat{\bar{G}}^{v,h}_{q,pr}(\mathbf{x}_B,\mathbf{x}_A,\omega \mid \mathbf{\Omega}) = \hat{\bar{G}}^{\tau,f}_{pr,q}(\mathbf{x}_A,\mathbf{x}_B,\omega \mid -\mathbf{\Omega}). \tag{A8}$$

Another choice is to represent both the sources in states *A* and *B* as deformation-rate sources, initiating wavefields at $\mathbf{x}_A$ and $\mathbf{x}_B$, respectively. The resulting expressions for the source and wavefield states are given in Table 6.

Substituting the states of Table 6 into equation (A7), making use of the properties of the delta functions and omitting the subscript $_r$, yields

$$\hat{\bar{G}}^{\tau,h}_{qs,p}(\mathbf{x}_B,\mathbf{x}_A,\omega \mid \mathbf{\Omega}) = \hat{\bar{G}}^{\tau,h}_{p,qs}(\mathbf{x}_A,\mathbf{x}_B,\omega \mid -\mathbf{\Omega}). \tag{A9}$$

In the time domain, equations (A4), (A6), (A8) and (A9), the generalized source-receiver reciprocity relations, read:

$$G^{\tau,\tau}_{qr,p}(\mathbf{x}_B,\mathbf{x}_A,t \mid \mathbf{\Omega}) = G^{v,h}_{p,qr}(\mathbf{x}_A,\mathbf{x}_B,t \mid -\mathbf{\Omega}), \tag{A10}$$

$$G^{v,\tau}_{q,p}(\mathbf{x}_B,\mathbf{x}_A,t \mid \mathbf{\Omega}) = G^{v,\tau}_{p,q}(\mathbf{x}_A,\mathbf{x}_B,t \mid -\mathbf{\Omega}), \tag{A11}$$

$$\bar{G}^{v,h}_{q,pr}(\mathbf{x}_B,\mathbf{x}_A,t \mid \mathbf{\Omega}) = \bar{G}^{\tau,f}_{pr,q}(\mathbf{x}_A,\mathbf{x}_B,t \mid -\mathbf{\Omega}) \text{ and} \tag{A12}$$

$$\bar{G}^{\tau,h}_{qs,p}(\mathbf{x}_B,\mathbf{x}_A,t \mid \mathbf{\Omega}) = \bar{G}^{\tau,h}_{p,qs}(\mathbf{x}_A,\mathbf{x}_B,t \mid -\mathbf{\Omega}). \tag{A13}$$

We can directly find the generalized acoustic source-receiver reciprocity relations by replacing the superscripts h by q, τ by $-p$ and leaving out all the subscripts. By doing so, the acoustic versions of equations (A10)–(A13) become

$$G^{p,p}(\mathbf{x}_B,\mathbf{x}_A,t \mid \mathbf{\Omega}) = G^{v,q}(\mathbf{x}_A,\mathbf{x}_B,t \mid -\mathbf{\Omega}), \tag{A14}$$

$$G^{v,p}(\mathbf{x}_B,\mathbf{x}_A,t \mid \mathbf{\Omega}) = G^{v,p}(\mathbf{x}_A,\mathbf{x}_B,t \mid -\mathbf{\Omega}), \tag{A15}$$

$$\bar{G}^{v,q}(\mathbf{x}_B,\mathbf{x}_A,t \mid \mathbf{\Omega}) = -\bar{G}^{p,f}(\mathbf{x}_A,\mathbf{x}_B,t \mid -\mathbf{\Omega}) \quad \text{and} \tag{A16}$$

$$\bar{G}^{p,q}(\mathbf{x}_B,\mathbf{x}_A,t \mid \mathbf{\Omega}) = \bar{G}^{p,q}(\mathbf{x}_A,\mathbf{x}_B,t \mid -\mathbf{\Omega}). \tag{A17}$$

In a non-rotating medium source-receiver reciprocity holds. The source-receiver reciprocity relations are derived similarly to the derivation of the generalized source-receiver reciprocity relations, equations (A4), (A6), (A8) and (A9) but leaving out the argument indicating the sense of rotation. Thus, the elastodynamic and acoustic source-receiver reciprocity relations are equations (A10)–(A13) and (A14)–(A17), respectively, without the argument indicating the sense of rotation.

APPENDIX B: ARTEFACTS

B.1. Imperfections

Some large imperfections in our finite difference-modelled response of state *B* are the model boundary artefacts. These low-frequency events can be seen in Fig. 6b.

With the dinite difference modelling (section 3), both the sources and the receivers were put at approximately 4 km depth. The resulting response of the model with free surface is not optimal. The measured amplitude varies from receiver (set) to receiver (set). These turned out to be large variations (2-10 km) in the source/receiver distance to the free surface, explaining the differences in amplitude in the measured responses.

The seismic interferometry algorithm itself is insensitive to mis-positioning of the sources. Normally the mis-positioning gives, e.g., a small delay for the events arriving at $\mathbf{x}_A$ and a small delay for the events arriving at $\mathbf{x}_B$. After correlation this time-delay is removed. Because of two (numerical) reasons, the mis-positioning of the sources does lead to errors in our numerical implementation, however.

The first reason is because sources are placed so close to the free surface, mis-positioning has an effect on the effective phase characteristic of the source wavelet. The phase characteristic of the source wavelet arriving at $\mathbf{x}_B$ does not change, though, as it is modelled independently in a model without free surface.

The second reason is that we used one receiver gather to make receiver gathers at all other epicentral distances. This has as an effect of traces correlating with each other which are not due to the same source but from sources with a different source (mis-)positioning.

B.2. Noise

According to the theory, by stacking over a correlation panel all amplitudes should interfere destructively, except for the physical events. We found that there was still some noise left, most obvious in Figs 11(a) and (b).

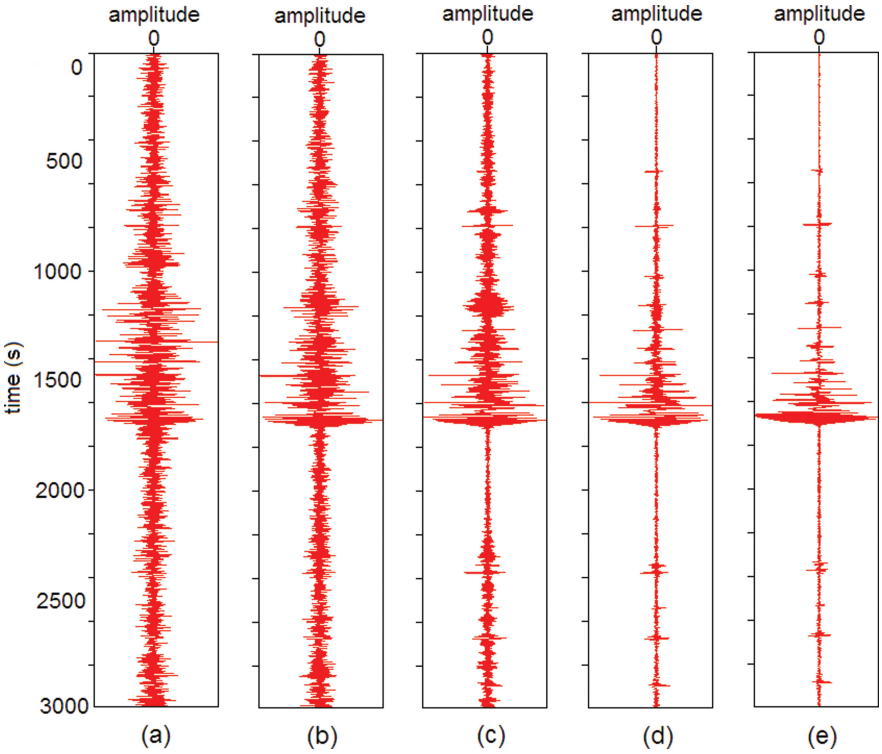

Figure 17 The reconstructed result using the seismic interferometry relation without near offset for $\mathbf{x}_A$ at 90° Δ from $\mathbf{x}_B$ with using respectively (a) 360, (b) 720, (c) 1440, (d) 2880 and (e) 5760 sources around the model.

To study the influence of the spatial sampling, we repeated the experiment as visualized in Figs 7 and 8 for five different source samplings. Figure 17 shows the reconstructed responses using the seismic interferometry relation without near offset when using (a) 360, (b) 720, (c) 1440, (d) 2880 and (e) 5760 sources around the model. This corresponds to one source every (a) 111, (b) 56, (c) 28, (d) 14 and (e) 7 km, respectively.

When using 360 sources (a), the 'real' events can hardly be seen through the noise. Using more and more sources, thus increasing the spatial sampling, more and more noise can be seen to disappear. In (e), when using 5760 sources, only a fraction of the noise is left. This number of sources corresponds with the Nyquist spatial sampling criterion for the used frequencies and the minimum velocity in the model.

Here, we have shown that the noise is a function of the source sampling. Thus, this noise is correlation noise, resulting from cross-correlations of all kinds of events that have not shared a common travelpath and thus does not lead to stationary phase events in the correlation panel. With a proper sampling the correlation noise almost completely disappears. The tiny amount left could be due to numerical errors as mentioned in the previous section.

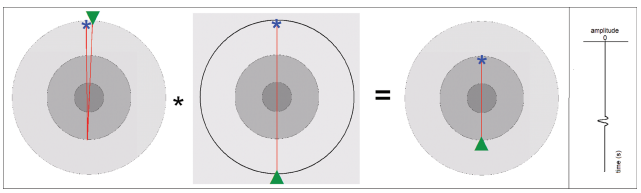

Figure 18 Correlation example. The drawings are models of the Earth. The red lines are ray paths of specific events that are measured at a receiver (green triangle) and initiated by a source nearby the Earth's surface (blue star). The correlation of a specific reflection response (drawn in the left-hand model) with a transmission response (middle model) results in an internal event (right-hand model). The trace on the right-hand side shows the phase-characteristic of the reconstructed event.

B.3. Additional events

Here, we analyse the occurrence of additional events. These are reconstructed events that are not in the finite difference-modelled response. These are sometimes referred to as spurious multiples or non-physical events. They are most obvious in the causal result (Figs 11a and b), but can also be seen in the anticausal result (Figs 10a and b).

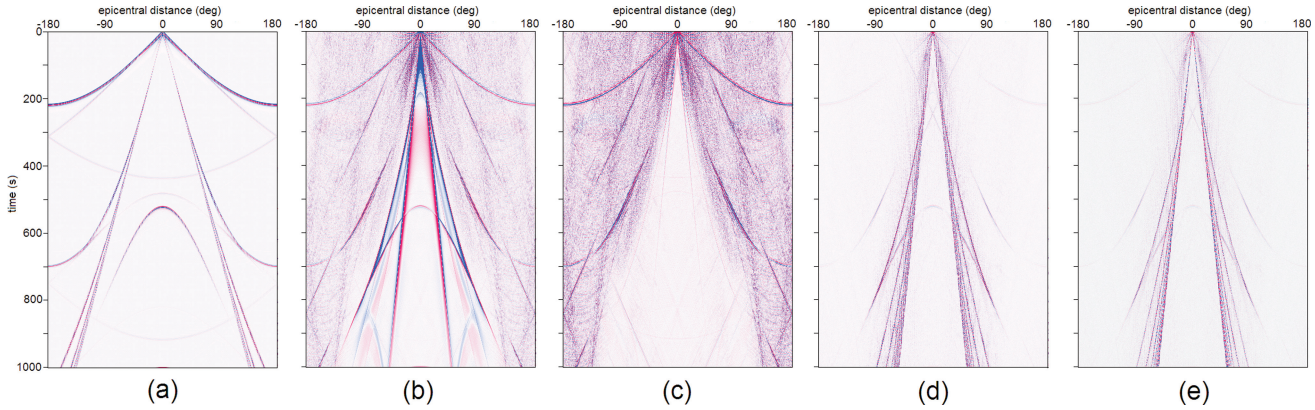

Figure 19 Comparison of the reconstructed additional events with the finite-modelled responses of internal events; (a) the finite difference-modelled internal events measured and initiated at the core-mantle boundary as well as measured and initiated at the inner core-outer core boundary; (b) is the causal reconstructed result; (c) is the causal result without near offset (as shown previously in Figs 11a and b); (d) is the time-reversed anticausal correlation result and (e) is the result without near offset (as shown previously in Figs 10a and b). The first 1000 s of the responses are shown because in this time window the additional events were most obvious.

One possibility to reconstruct such an additional event would be by a correlation of events as indicated on Fig. 18. We assume an Earth with two velocity contrasts (core-mantle boundary and inner core-outer core boundary), indicated with different levels of grey in the 2D Earth models. A reflection in state *A* is correlated with a transmission in the computational state *B* resulting in an event with the kinematics as if there is a source at the core-mantle boundary and a direct transmission was measured by a receiver, also at the core-mantle boundary. On the right-hand side the phase characteristics of the reconstructed event is given, assuming a first derivative Gaussian source wavelet. We call such an event, which is both initiated and measured at a boundary within the Earth, an internal event.

To test whether the additional events are actually internal events, we forward-model the response for one source at the core-mantle boundary and register the response at receivers placed around the core-mantle boundary. Also, we place a source at the inner core-outer core boundary and measure the response at the same boundary. We plot the responses measured at the core-mantle boundary upon the responses measured at the inner core-outer core boundary, resulting in Fig. 19(a). This combined response is compared with our previous reconstructed response (Figs 10 and 11). Figures 19(b), (c), (d) and (e) depict the first 1000 s of the causal reconstructed result, the causal result without near offset, the time-reversed anticausal correlation result and the anticausal result without near offset, respectively. It can clearly be seen that the additional events in the causal results indeed have the same kinematics as the events modelled in Fig. 19(a). The additional events in the anticausal result are less visible but follow the same kinematics.

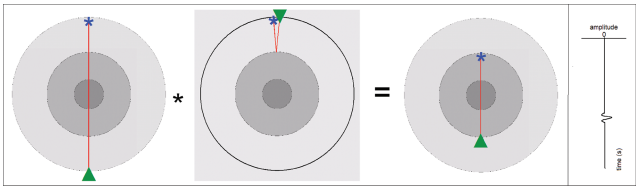

Figure 20 Correlation example. The drawings are models of the Earth. The red lines are ray paths of specific events that are measured at the free surface (FS) (green triangle) and initiated by a source nearby the Earth's surface (blue star). The correlation of a transmission response (drawn in left-hand model) with a specific reflection response (middle model) gives an internal event (right-hand model). The traces on the right-hand side show the phase-characteristic of the event reconstructed.

From the above test it can be concluded that the additional events are (mainly) internal events that follow from a correlation of events as depicted in Fig. 18.

According to the derived relations for seismic interferometry, though, no additional events are predicted. Hence, when the conditions assumed during the derivation of these relations are fulfilled, the additional events should not appear.

With a similar example, as in Fig. 18, we can also explain how these additional events could disappear. In Fig. 20 a transmission in state *A* is correlated with a reflection in state *B* resulting in an event with the kinematics as if there is a source a the core-mantle boundary and a direct transmission was measured by a receiver, also at the core-mantle boundary.

On the right-hand side the phase characteristics of the reconstructed event is given, assuming a first derivative Gaussian source wavelet. Now comparing Figs 18 and 20 we see that the reconstructed events have precisely opposite phase characteristics. The summation of both correlation results should cancel these internal events.

Analysing correlation panels (e.g., as depicted in Fig. 8) it can indeed be seen that these additional events have stationary phase events with an opposite phase characteristic. Hence, as the theory predicts and as can be intuitively understood by a simple analysis as above, with a perfect source sampling (perfect illumination from all sides), with no losses within the model and with sufficiently long input responses, these additional events will cancel each other out. In our case, it is especially the use of an input duration for which all possible internal multiples have not yet been recorded for state *B* that leads to unequal amplitudes of stationary phase events with opposite phase characteristics. Let us explain. Suppose we call the reconstructed internal event on the right-hand side in Fig. 20 'K+'. There is only one way to retrieve K+, that is by a correlation of PKP and PcP, as illustrated in Fig. 20. Suppose we call the reconstructed internal event on the right-hand side in Fig. 18 'K−'. Figure 18 is an illustration of only one possibility to retrieve K−, that is by a correlation of PKKP and PKP. However, a correlation of P3KP and PKKP also gives K− and a correlation of P4KP and P3KP gives K−, etc. The amplitude with which we retrieve K− is thus a function of the recording length, or the order of P*KP that we include. With our modelling we do not use higher orders than P5KP, while higher orders still have significant amplitude. Thus, the sum of K+ and K− is still a significant deviation from zero.

For real data, the sampling of opposite stationary phase events that should cancel each other out will never be identical. Also, the amplitudes will not be equal because of (different) losses and the duration of the input responses will always be limited. Hence, the (partial) reconstruction of these internal events will be an issue. If we know *a-priori* where the large contrast exits, we can model where the stationary phases of these internal events will occur in the correlation panels and filter them out.

Besides being a nuisance, these additional events could bring unprecedented possibilities. One of the stationary phase events can be selected and hence a response could be constructed as if induced and measured at, e.g., the core-mantle boundary.